J. Fluid Mech. (1977), *vol.* 80, *part* 1, *pp.* 49–80
Printed in Great Britain

The near field in the mixing of a round jet with a cross-stream

By Z. M. MOUSSA,
Carrier Corporation, Syracuse, New York 13201

JOHN W. TRISCHKA
Department of Physics, Syracuse University, New York 13210

AND S. ESKINAZI
Department of Mechanical and Aerospace Engineering,
Syracuse University, New York 13210

(Received 29 January 1976)

In the mixing of a jet with a cross-stream, it is found that in the near field, defined as the region of the flow from the jet exit to a distance of a few diameters downstream of this exit, a considerable amount of dynamical adjustment takes place. This near-field region characterizes the subsequent behaviour and development of the jet, its wake and the cross-stream in the vicinity of this mixing region. The rapid evolution of the flow gives rise to a pair of bound vortices attached to the lee side of the jet boundary, to fast development of the turbulent and mean vorticity, to a vortex-shedding system, and to the largest rates of entrainment of cross-stream flow into the jet. Furthermore, it is found that the geometrical configuration of the boundaries at the jet exit plays an important role in the mixing and development processes.

An intrinsic method is proposed for the delineation of the flow boundaries between the jet and the cross-stream. Calculations of mass, momentum and vorticity fluxes have been made. The vorticity flux gives evidence of the rapid stretching and tilting of the vorticity vector field in the near-field region.

1. Introduction

Some atmospheric phenomena whose understanding may be improved through studies of a jet in a cross-wind are those involving thermal plumes generated at the earth's surface and rising to levels at which a significant cross-wind exists. Although buoyancy is the upward driving force in these flows, they will have many important dynamical features in common with isochoric jets.

Wake turbulence has been observed downwind of updrafts in thunderstorm systems. Observations indicating that the updrafts act as obstacles to the horizontal air flow were reported by Fankhauser (1971). The bound vortices identified in the present paper seem to play an important role in the development of clouds observed by Fujita & Grandoso (1968), and by Fankhauser, to split into clouds rotating in opposite directions. Shed vortices are commonly observed

downwind of forest fires (Whittingham 1959) and may be the result of vortex shedding from the rising plume of hot air. Whirlwinds and waterspouts observed downwind of volcano plumes (Thorarinsson & Vonnegut 1964) show some of the properties of shed vortices. Vortex streets observed, through satellite photography, in clouds below the inversion layer downwind of subtropical islands have been attributed by Chopra & Hubert (1964) to orographic effects, but may also be a consequence of updrafts and downdrafts related to mountain peaks on these islands.

Various forms of mixing of a round jet with a cross-stream can be found in a number of industrial applications. The flow issuing from a smoke stack in a horizontal wind has been of great interest owing to environmental implications. It is also known that at take-off and landing of VTOL aircraft, when the axis of the engine makes an angle with the wind, the mixing of the exhaust gases with the wind falls in the realm of this problem. In addition there are many combustion applications that require the mixing of two streams at right angles.

There does not exist agreement in the literature concerning the universal behaviour in the dynamics of plumes and jets in cross-streams, although systematic investigations of these flows began nearly forty years ago with those by Sutton (1932) and by Bosanquet & Pearson (1936). The methods of investigation used are essentially one-dimensional or two-dimensional in nature and can be summarized as follows: fitting empiricism to experimental measurements of plume shape and rise (Bosanquet & Pearson 1936; Lucas 1958; Holland 1953); using dimensional reasoning and fitting experimental results of special laboratory models (Hewett, Fay & Hoult 1971; Pratte & Baines 1967; Kamotani & Greber 1972), and using theoretical methods and assuming special idealized flow conditions such as top-hat velocity profiles, the linear entrainment suggested by the circular jet, and axisymmetry in the entire development (Morton, Taylor & Turner 1956; Priestley 1956; Laikhtman 1961; Turner 1969; Fay 1973).

The lack of universal agreement in these analyses seems to stem from two important factors. First, the initial conditions of the flow at the jet exit play a major role in the entrainment and, subsequently, in the development of the flow. Second, the mixing of a jet in a cross-stream, being essentially a three-dimensional vortical flow, does not lend itself to two-dimensional mathematical treatment. The essential motivation for the present work is the need to provide physical evidence related to these important factors.

2. Physical description of the jet in a cross-stream

A composite diagram of the mixing of a uniform parallel cross-stream with velocity U_∞ and an isochoric flow issuing from a round pipe of outside diameter D with an average exit velocity U_j is shown in figure 1. The co-ordinate system (x, y, z), the velocity components U, V and W, and the pitch and yaw angles of the velocity vector are shown. All distances are measured from the centre of the pipe exit.

The uniform cross-stream decelerates as it approaches the jet boundaries as if its passage were blocked by a rigid obstacle, the difference being that the

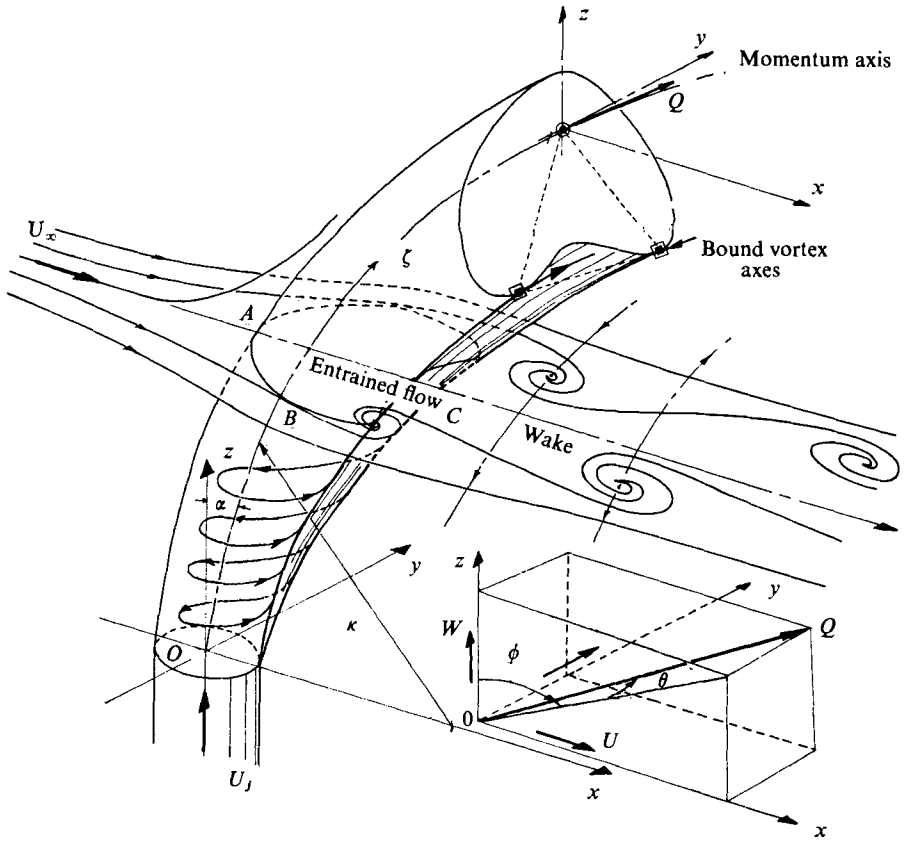

FIGURE 1. Flow description and co-ordinates.

boundaries of the jet are compliant and entraining. Figure 2 shows our results for the overall velocity and its components along $x' = x/D$ at $z' = z/D = 1{\cdot}00$ on the symmetry plane $y' = y/D = 0$. The velocity distribution of the cross-stream along the leading-edge streamline is compared with that of a flow around a rigid circular cylinder with diameter $1{\cdot}5D$, which is approximately the maximum width of the deformed jet at $z' = 1{\cdot}00$. The basic difference between the two profiles can be easily reconciled by a shift of the jet's leading edge by an amount of $\frac{1}{4}D$ at the elevation $z' = 1{\cdot}00$. For higher values of z', the angle $\frac{1}{2}\pi + \alpha$ between the jet axis and the direction of the cross-stream cannot be ignored. In figure 1, as the cross-stream approaches the jet boundary and decelerates, it deflects around the boundary surface AB with partial mixing with the jet flow. The experimental results show that the V component from A to B is everywhere outward while the U component of the cross-stream increases around the boundary AB, much the same as around a rigid cylinder of the same cross-section. Figure 3 shows that the U distribution reaches approximately its maximum value of $U_{\max}/U_\infty = 2{\cdot}0$ at the two planes $z' = 0{\cdot}50$ and $1{\cdot}00$, where the jet angle α is still very small, as in the case of a rigid cylinder.

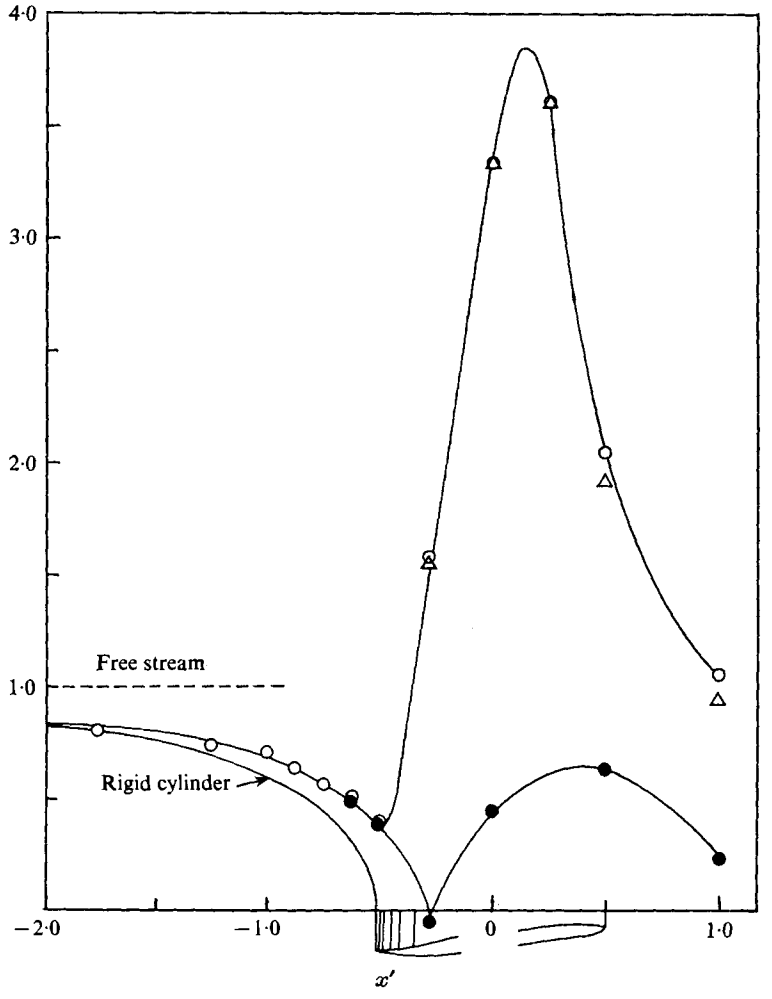

FIGURE 2. Pseudo-stagnation streamline ($y' = 0, z' = 1{\cdot}00$); $V/U_\infty = 0$ (symmetric). ○, Q/U_∞; ●, U/U_∞; △, W/U_∞.

In the wake region BC a number of important effects take place. Most of the mean vorticity issuing from the pipe, tilted and stretched by the flow, bundles up into a pair of vortex tubes bound to this lee surface of the jet. Furthermore, a portion of this mean pipe vorticity and the additional vorticity generated at the interface of the two flows rolls up into periodically shed vortices similar to those in the von Kármán–Bénard street. Together, these two vortex systems are responsible for most of the entrainment of cross-stream flow into the deflected jet and its wake. Also, in this region a significant amount of the initial pipe vorticity is converted into turbulent vorticity through the action of the Reynolds stresses.

It is important to note at this point that the presence or absence of a rigid wall, in the x, y plane, at the jet exit is crucial to the behaviour of the whole flow, particularly in the near field. In other words, the results of the mixing of a uniform

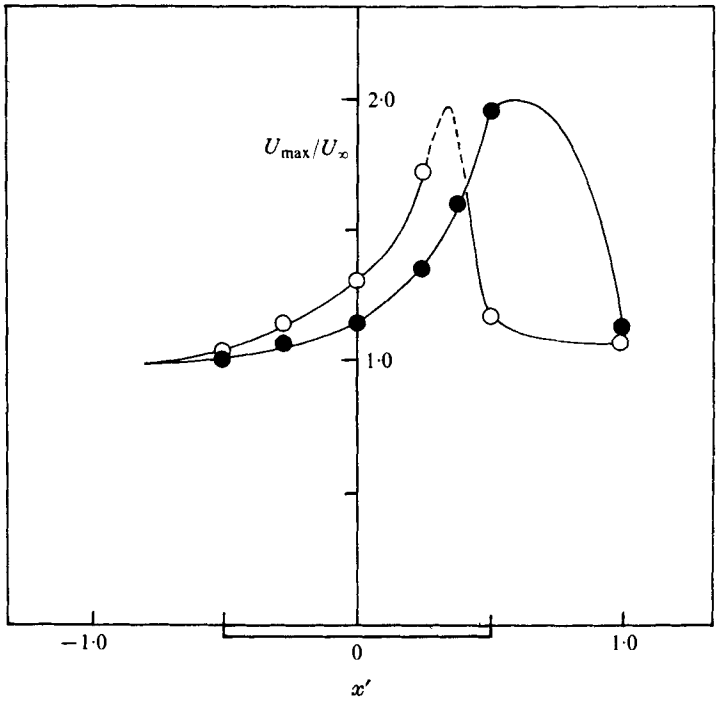

FIGURE 3. Locus of maximum U/U_∞ around the jet boundary. ○, $z' = 0{\cdot}5$; ●, $z' = 1{\cdot}00$.

stream with a flow from a hole in a wall, with that from a pipe with a flat-plate skirt at the plane of discharge and with that from a simple pipe will be quite different. The initial vorticity at the jet discharge for a hole in a wall will be different from that for a pipe discharge. Second, for the case of a hole in a wall and a skirted pipe, the vorticity Ω distributed in the boundary layer over the wall or skirt will also roll up, as it separates past the stagnation point, and affect the bound vortex system. Also, in the absence of a skirt at the pipe exit, the Helmholtz law on vortex-line continuity must prevail, and vortex shedding behind the rigid pipe must be continuous with that behind the jet. This will be demonstrated in § 5.2. For a skirted pipe, the skirt will make it possible for the two shedding systems, below and above it, to be independent.

3. Experimental equipment and procedure

A pipe 2·54 cm O.D., 2·36 cm I.D. and 61 cm long located inside a rectangular test section of an air tunnel provided the flow of air for the jet. The spatial mean velocity at the pipe exit was $U_j = 29{\cdot}6$ m/s. In order to avoid buoyancy effects, the temperatures of the jet and the cross-stream were kept within 1 °C with the help of an air conditioner in the supply line of the jet. All the results in this paper pertain to this isochoric mixing with $U_j/U_\infty = 3{\cdot}48$, except for the shedding measurements in § 5.2. The cross-stream velocity was $U_\infty = 8{\cdot}5$ m/s, in a low

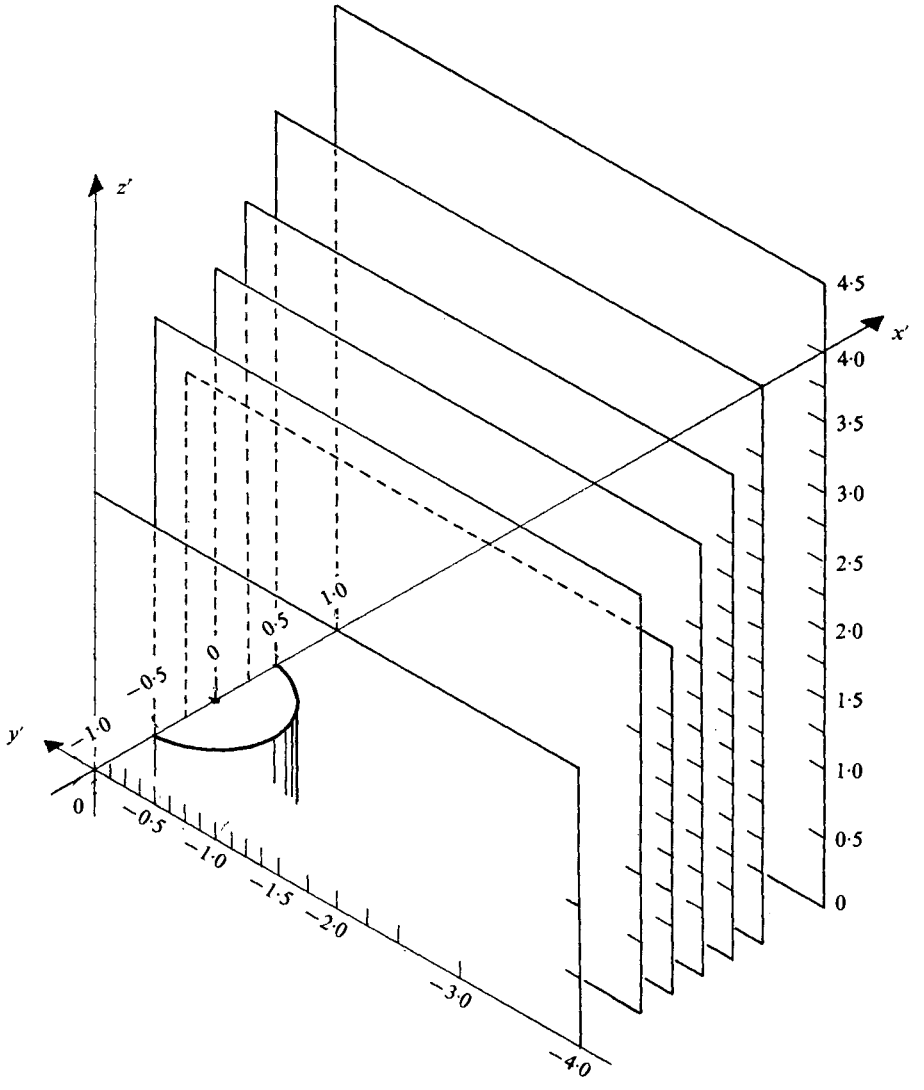

FIGURE 5. The three-dimensional matrix array of measurement points.

turbulence (1·2 %) tunnel 1·22 m high by 0·61 m wide and 6 m long. To simulate a natural environment, the tunnel walls diverged slightly to maintain a constant static pressure. The ratio of the pipe diameter to the tunnel dimensions was small, and the jet exit was kept far away from the tunnel walls at all times. Figure 4 (plate 1) shows the tunnel set-up.

As the flow was three-dimensional, the mean angles were measured with a United Sensor three-dimensional probe 3·2 mm in diameter. This probe was calibrated in a special directional tunnel. The temporal mean velocity and turbulence levels were measured with a linearized DISA Constant-Temperature Anemometer after the wire had been oriented normal to the mean flow. The turbulent fluctuations were processed electronically to provide r.m.s. values,

one-dimensional spectra, shedding frequencies and scales of turbulence. The wires were 5 μm in diameter and 1·25 mm in length. The mean voltage was read with a Hewlett–Packard D.C. Digital Voltmeter, the r.m.s. value on a Ballantine True R.M.S. Voltmeter, the spectral densities with a General Radio Third Octave Real Time Analyzer, and the shedding frequencies with a Spectral Dynamics Narrow Band Real Time Analyzer with 3 Hz constant bandwidth.

Figure 5 shows the three-dimensional array of measured points in this study. Every graduation in the co-ordinates x', y' and z' corresponds to a measured point. The total number of measured points was in the vicinity of 1000.

4. Similarity considerations

Similarity relations can be established from the x component of the Navier–Stokes equation and from simple radial equilibrium in the direction κ normal to ζ shown in figure 1. They may be approximated as

$$\partial P/\partial \kappa \simeq \rho_j U_j^2/\kappa, \tag{1}$$

where P is the pressure, ρ the density and κ the radius of curvature of the bent jet. This radial pressure gradient can be related to the pressure gradient in the x direction through multiplication by cos α. When one considers the flow outside the jet, including the transient wake, which is partly periodic owing to shedding and partly irregular owing to turbulence, the x component of the Navier–Stokes equation can be made dimensionless as follows:

$$\frac{fL}{U_\infty}\frac{\partial U_*}{\partial t_*} + U_*\frac{\partial U_*}{\partial x_*} + \ldots = -\frac{\rho_j}{\rho_\infty}\frac{L}{\kappa}\left(\frac{U_j}{U_\infty}\right)^2 \cos\alpha + \frac{\nu}{U_\infty L}\left(\frac{\partial^2 U_*}{\partial y_*^2} + \ldots\right), \tag{2}$$

where $U_* = U/U_\infty$, $t_* = t/\tau$, $x_* = x/L$ and $y_* = y/L$, while τ and L are the characteristic time and length scales, f is the frequency in the transient wake and ν is the viscosity.

For two of these flows to be geometrically, kinematically and dynamically similar, each of the dimensionless terms in this equation must be the same for the two flows. This implies that the coefficients

$$\frac{fL}{U_\infty}, \quad \frac{\rho_j}{\rho_\infty}\frac{L}{\kappa}\left(\frac{U_j}{U_\infty}\right)^2 \cos\alpha, \quad \frac{\nu}{U_\infty L} \tag{3}$$

must be the same. The bending geometry of the jet, expressed by L/κ and α, must be the same and can be related directly to the momentum flux ratio of this flow (Eskinazi 1975). The momentum flux per unit area of the uniform cross-stream is $\rho_\infty U_\infty^2$ while the momentum flux of the jet is

$$2\pi \int_0^{\frac{1}{2}D'} \rho_j W_j^2 r\, dr,$$

where W_j is the local velocity at the pipe exit. At a given distance x' downwind of the pipe exit κ/D', α and L/D' will have specific values and the momentum ratio of the two streams can be expressed in terms of

$$\frac{\pi\rho_\infty U_\infty^2 L^2}{2\pi\rho_j \int_0^{\frac{1}{2}D'} W_j^2 r\, dr} = \beta\frac{\rho_\infty}{\rho_j}\left(\frac{U_\infty}{U_j}\right)^2\left(\frac{L}{D'}\right)^2, \tag{4}$$

	Inside pipe $D = 2{\cdot}54$ cm (O.D.)	Measured flow just outside the pipe $z' = z/D = 0{\cdot}04$
Flow diameter (cm)	$D' = 2{\cdot}36$ (I.D.)	2·56
Area (cm^2)	4·37	—
Volume flow rate, ϕ_j(m^3/s)	0·013	0·013
Space average velocity (m/s)	$U_j = 29{\cdot}6$	25·0
Shape factor, β	1·085	1·085
Bulk momentum flux (m^4/s^2)	0·42	0·35
Kinematic viscosity (m^2/s)	$1{\cdot}58 \times 10^{-5}$	$1{\cdot}58 \times 10^{-5}$
Density (kg/m^3)	1·15	1·15
Jet Reynolds number, R_j	$4{\cdot}40 \times 10^4$	—
x vorticity flux, $\phi_{\Omega jx}$ (m^3/s^2) (half-flow)	—	10·6
Absolute vorticity flux, $\phi_{\Omega j}$ (m^3/s^2) (half-flow)	—	16·6
Spatial mean vorticity, $2\phi_{\Omega j}/AU_j = \Omega_j$ (s^{-1})	—	2570

Free-stream velocity $U_\infty = 8{\cdot}5$ m/s, $R_\infty = 1{\cdot}36 \times 10^4$, $J = 12{\cdot}1$

TABLE 1. Basic and initial flow parameters.

where D' is the inside diameter of the pipe and where β is the *shape factor* or the ratio of the momentum flux at the jet exit to the momentum flux of the mean flow at the same exit, equal to $\frac{1}{4}\pi D'^2 U_j^2$. From free-jet theory L/D' will be dependent on $R_j = U_j D'/\nu$. Thus from (3) and (4) we conclude that the initial dimensionless ratios that govern similarity in this non-buoyant flow are

$$S = \frac{fD}{U_\infty}, \quad J = \left(\frac{U_j}{U_\infty}\right)^2, \quad R_\infty = \frac{U_\infty D}{\nu}, \quad R_j = \frac{U_j D'}{\nu}, \quad \beta. \tag{5}$$

With the exception of the Strouhal number S, which will be discussed in § 5.2, all these quantities are listed in table 1, as the initial conditions of the flow.

The pipe was not long enough to generate a fully developed flow. The pipe exit conditions were measured 1 mm downstream of the pipe exit, corresponding to $z' = 0{\cdot}04$. It was assumed that the shape factor remained the same in that small distance. Strictly speaking, this may not be true because the wall shear is suddenly relaxed, and this is accompanied by a momentum change. Values in table 1 have been used to make the results of this investigation dimensionless.

5. Rolling-up and initial pipe vorticity

5.1. *The bound vortex system*

Before the exit, the pipe flow is everywhere in the z direction and the vorticity is everywhere in the x, y plane, normal to the radial direction. Thus the velocity and vorticity vectors are normal to each other. The mean vortex lines are concentric rings with the largest value of the vorticity at the pipe wall. In the near field it becomes important to determine the behaviour of these rings as they emerge from the pipe. This behaviour can be explained through the special form of the convective acceleration **a**:

$$\mathbf{a} = (\mathbf{Q}\cdot\nabla)\mathbf{Q} = \tfrac{1}{2}\nabla Q^2 - \mathbf{Q}\times\boldsymbol{\Omega}, \tag{6}$$

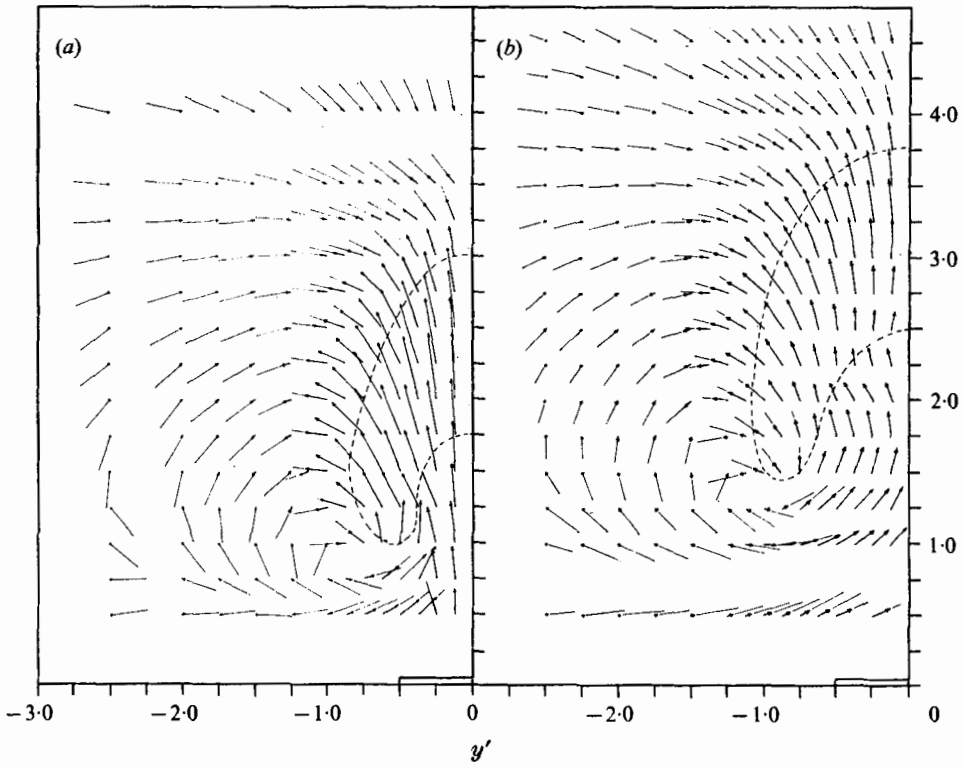

FIGURE 6. Velocity projection Q_z/U_j on planes normal to x. (*a*) $x' = 0{\cdot}50$. (*b*) $x' = 1{\cdot}00$.

where $\mathbf{Q}$ is the velocity and $\boldsymbol{\Omega}$ the vorticity. The two components of the term $\frac{1}{2}\nabla Q^2$, in a free jet, are radially inward and axially opposing the mean motion. The larger term $-\mathbf{Q}\times\boldsymbol{\Omega}$ is radially outward. Hence the free jet expands radially with axisymmetry and decelerates at the same time.

With a cross-stream, owing to the bending of the jet, the plane of the vortex rings soon becomes inclined at an angle ψ to the resultant velocity $\mathbf{Q}+\mathbf{U}_\infty$. Reviewing the geometry of the acceleration terms, in this case, Eskinazi (1975) showed that this angle ψ will give in the cross-product a radial component which is symmetric (as in the case of the free jet) and equal to

$$|-\mathbf{Q}+\mathbf{U}_\infty||\boldsymbol{\Omega}|\cos\psi = |-\mathbf{Q}\times\boldsymbol{\Omega}|,$$

and an axial component

$$|-\mathbf{Q}+\mathbf{U}_\infty||\boldsymbol{\Omega}|\sin\psi = |\mathbf{U}_\infty\times\boldsymbol{\Omega}|$$

which is asymmetric because of its dependence on the sine of the angle. The resultant radial component $-\mathbf{Q}\times\boldsymbol{\Omega}+\frac{1}{2}\nabla_r Q^2$ will spread these rings in a symmetrical way as in the case of the free jet, while the resultant axial component $\mathbf{U}_\infty\times\boldsymbol{\Omega}+\frac{1}{2}\nabla_z Q^2$ will have its maximum negative value on the windward side of the ring and definitely larger positive values on the lee side, owing to the fact that $\mathbf{U}_\infty\times\boldsymbol{\Omega}$ is positive there. The values of this axial component at the sides of the ring will be the same.

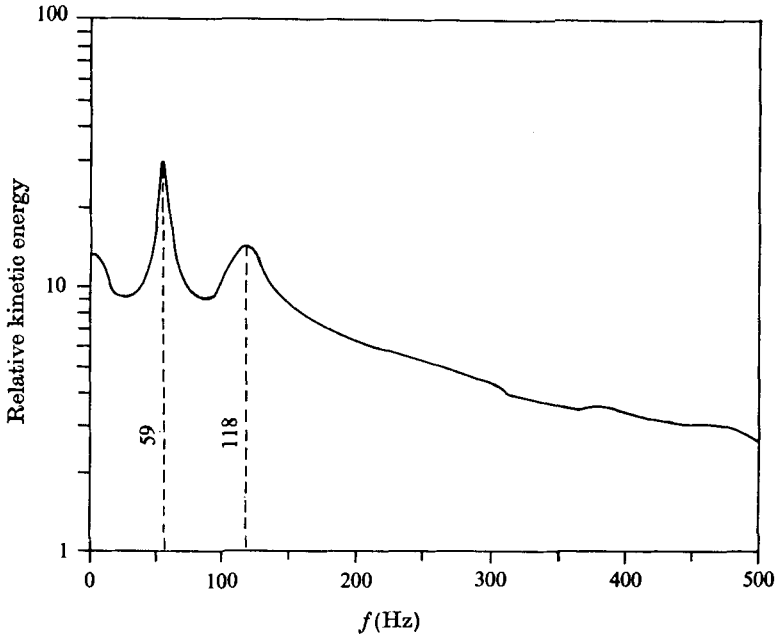

FIGURE 7. Energy distribution in the shedding process.

In time, the ring will be swept with the fluid, decelerating on the windward side faster than at the centre and accelerating relatively on the lee side. This situation will persist with diminishing intensity during the entire development of the deflected jet as it asymptotically approaches a Beltrami flow, for which $\mathbf{Q} \times \boldsymbol{\Omega} = 0$. Each successive ring will do the same, so that on the lee side these rings will bundle up into two bound vortex tubes joined at infinity, making two counter-rotating helical spiral motions much like the tip vortices of aeroplane wings. It must be emphasized that the major part of the change from complex lamellar flow ($\mathbf{Q} \cdot \boldsymbol{\Omega} = 0$) to Beltrami flow takes place in the vicinity of the pipe exit.

Measurements of the three-dimensional velocity field, in the initial stages of the flow, and the calculated three-dimensional vorticity field support this behaviour. First, the two plots in figure 6 of the velocity projection

$$Q_x = (V^2 + W^2)^{\frac{1}{2}}$$

on planes $x' =$ constant show this development of the bound vortex for the planes $x' = 0{\cdot}50$ and $1{\cdot}00$. Since the arrows shown in the figure are projections of the velocity vector, streamlines should not be inferred. The flow field is strongly three-dimensional and the streamlines, as well as having swirl in these planes, advance in the direction normal to the paper. The contours of V/U_∞ in figure 14 also support the presence of the bound vortex on the lee side of the jet.

5.2. *The shed vortex system*

Analysis by the narrow-band spectrum analyser of the hot-wire output showed that, in addition to turbulence, shedding of a von Kármán–Bénard vortex street occurred. Figure 7 is a typical wake energy spectrum, the largest peak

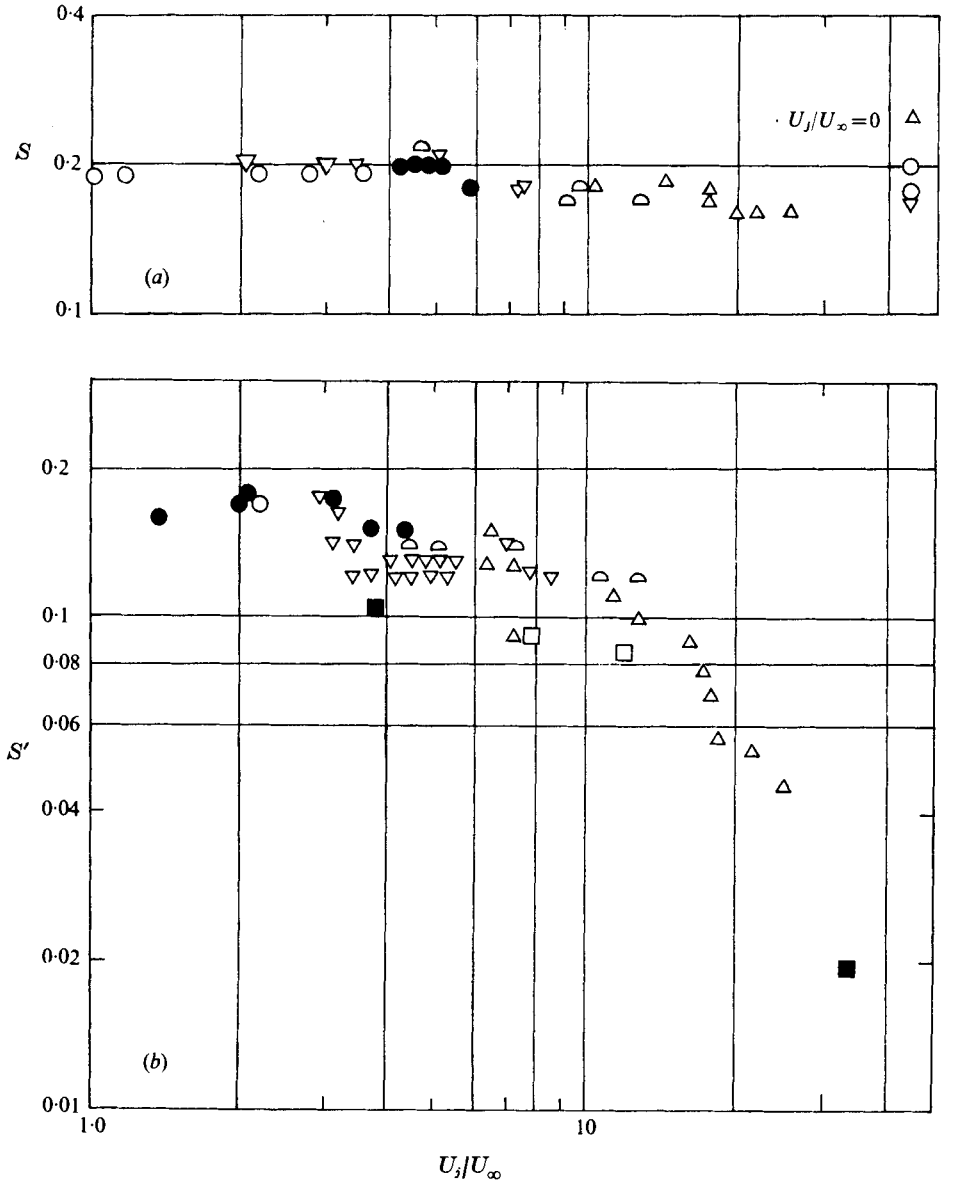

FIGURE 8. The shedding phenomenon. (*a*) No skirt; $S = fD/U_\infty$. (*b*) Skirt on; $S' = fD'/U_\infty$. Present results: ○, $R_\infty = 16000$; ●, $R_\infty = 12000$; ▽, $R_\infty = 8000$; ⌓, $R_\infty = 5000$; △, $R_\infty = 3000$. ■, McAllister (1968); □, McMahon *et al.* (1971).

corresponding to the shedding from one side of the jet. The secondary peak, at exactly twice the frequency, appears when the hot wire is in the vicinity of $y' = 0$. This is the result of sensing vortices alternately shed from both sides of the jet.

Figure 8 shows the variation of the Strouhal number for the shed vortices as a function of the velocity ratio U_j/U_∞. The upper curve on the figure shows data taken in the wake of the jet from a simple pipe issuing into a cross-stream. The

lower curve shows data from an experimental arrangement in which a flat rectangular metal plate or 'skirt' was mounted flush with the pipe's upper edge. The plate had a streamwise length of 0·32 m, a cross-stream (y direction) width of 0·25 m and a thickness of $1{\cdot}6 \times 10^{-3}$ m. The distance from the centre of the pipe to the leading edge of the skirt was 0·064 m. Note that $S = fD/U_\infty$ is plotted for the unskirted pipe and $S' = fD'/U_\infty$ for the skirted pipe.

For the case of the unskirted pipe there seem to be two regimes, the change from one to the other occurring near $U_j/U_\infty = 5{\cdot}5$. Also, there is evidence that shedding from the jet above the unskirted pipe is dominated by shedding from the solid pipe because of the apparent lack of dependence of S on R_∞ and U_j/U_∞. This is because the same shedding frequencies are measured in the jet wake as in the pipe wake, and ultimately because of the shape of the resonance curve. The latter reason requires further explanation. For $U_j/U_\infty < 5{\cdot}5$, for the unskirted case the ratio of the frequency width at the half-maximum of the shedding peak to the centre frequency is about 0·1, whereas the same ratio for the jet above the skirted pipe is two to four times larger. The width of the resonance curve is a result of random fluctuations from strict periodicity. The spread of these fluctuations should be greater from a jet than from a solid cylinder because of the turbulence at the jet boundary. For $U_j/U_\infty > 5{\cdot}5$ in the unskirted case the width of the resonance curve increases and the Strouhal number decreases. This indicates that the jet properties begin to influence the Strouhal number of the pipe–jet system.

The shedding in the skirted case seems also to be characterized by two regimes, the change in regime occurring in this instance near $U_j/U_\infty = 3$. The results of McAllister (1968), who used a water tunnel, and of McMahon, Hester & Palfrey (1971), who experimented with air, seem to agree with the current data for the skirted pipe. From the similarity considerations summarized in (5) one should expect that, for a given β, S should be a function of R_∞ and U_j/U_∞. These considerations should apply in only a minor way to the unskirted case, where the pipe dominates the shedding.

The data for the skirted case largely support the conclusion that the shedding is nearly independent of R_∞. At $U_j/U_\infty = 12$, McMahon *et al.* found no change in S' when R_∞ was changed from 52 000 to 26 000.

6. Jet boundaries

As in the case of any turbulent mixing process involving one or more streams, the mixing process here has no sharply defined boundaries. The changes in the flow properties and their derivatives are continuous. Nevertheless, some derivatives have typical behaviours that can be used as a criterion for defining a boundary. The schematic diagram in figure 1 shows three distinct regions in the entire flow: the free stream, the deflected jet and the wake, which in turn can be divided into three main parts, namely the turbulent wake due to separation and shear on the surface of the jet, the shedding wake due to the rolling-up of some of the mean vorticity at the boundary surface, and the bound vortex system attached to the trailing surface of the jet, which is reponsible for the entrainment of free-stream and wake fluid into the jet.

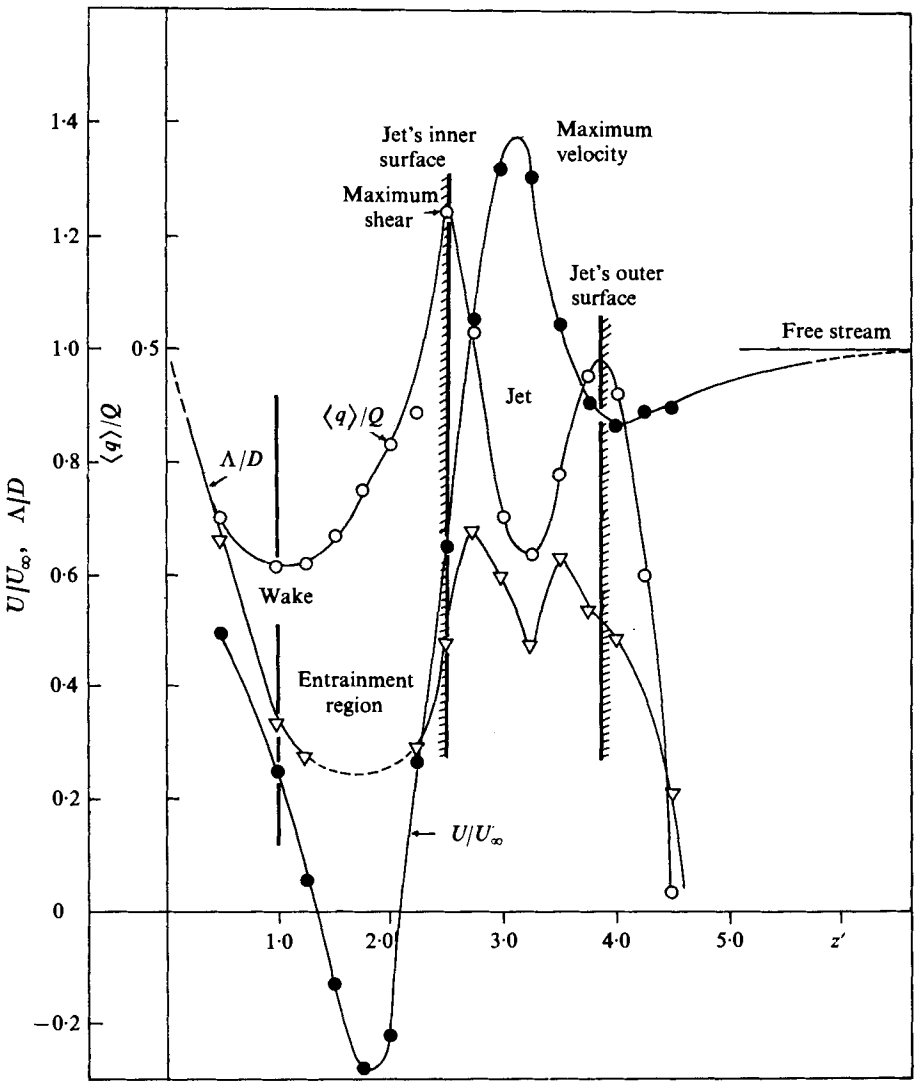

FIGURE 9. Delineation of special regions along the line $x' = 1{\cdot}00$, $y' = 0$.

Figure 9 illustrates these regions. It shows a traverse from wake to free stream, in the plane $x' = 1{\cdot}00$ for $y' = 0$, of the following physical quantities serving to delineate the various regions: the turbulence level $\langle q\rangle/Q$, the velocity distribution U/U_∞ and the macroscale of the turbulence Λ/D. From the following comparative behaviours of these distributions, a consistent method of defining the boundaries of the regions is proposed. Because of symmetry, Ω_x vanishes at $y' = 0$ and therefore cannot be used as a comparative criterion in this plane. In figure 9 the $\langle q\rangle/Q$ distribution shows two peaks associated with regions of maximum shear. The first peak, at $z' \simeq 2{\cdot}5$, is the shear region between the wake and the jet. The U/U_∞ distribution also shows a large shear at this point. It is expected also that the magnitude of the total vorticity is a maximum near this point. Strictly

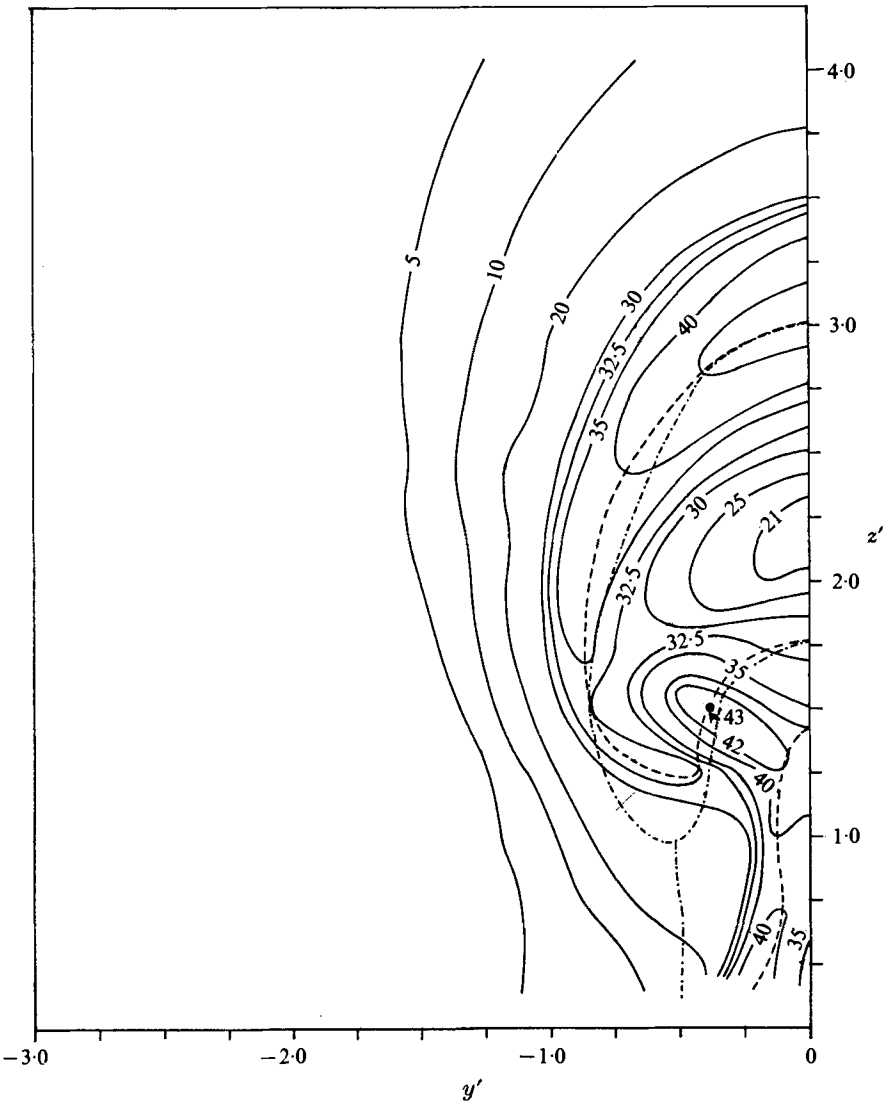

FIGURE 10. Contours of 100 $\langle q \rangle / Q$ and maximum vorticity ridge on the plane $x' = 0{\cdot}5$. –·–, vorticity ridge; – – –, turbulence ridge.

speaking, the maximum turbulence, shear and mean vorticity do not necessarily occur at the same point but they are sufficiently near to choose one of the maximum values to define a characteristic boundary. Figure 10 shows the contours of $\langle q \rangle / Q$ in the plane $x' = 0{\cdot}5$, where total vorticity values are also available. On this figure the ridges of turbulence and vorticity are also plotted, and may be seen to be nearly compatible. We need to emphasize, however, that $\langle q \rangle / Q$ values represent only that portion of the turbulent kinetic energy in the direction of the mean motion, whereas the vorticity ridge is based on the total vorticity. It is for this reason that we choose *to define the boundaries of the jet by the ridge of the vorticity*. Hence, at $y' = 0$ the wake is in the region $0 < z' < 2{\cdot}5$

on the $x' = 1{\cdot}00$ plane of figure 9. Also in the region $1{\cdot}00 < z' < 2{\cdot}5$ the x component of the velocity is small and negative, i.e. in the direction opposite to that of the free-stream flow. This is the *entrainment region* of the wake, where the flow is in fact inward with reference to the jet boundaries.

As one crosses the inner boundary in figure 9, i.e. for $2{\cdot}5 < z' < 3{\cdot}75$, the velocity U/U_∞ reaches a maximum, while $\langle q \rangle/Q$ and Λ/D drop to another minimum. This region is characterized as the jet proper, the properties displaying similar behaviour to those in the free jet. At $z' = 3{\cdot}75$ the turbulence level reaches another maximum, delineating the *outer boundary of the jet*, while the mean velocity rises asymptotically to the free-stream value. Because of the presence of the jet, the free stream remains deflected for a significant distance z' beyond this outer boundary. Also, in figure 9 the macroscale extrapolates, at $z' = 0$, to the value of the pipe diameter.

7. The general development of the flow

The important effect of the geometrical configuration at the jet discharge on the flow development has already been discussed briefly in § 2, but needs to be enlarged upon at this point. One finds considerable variations in the literature in the experimental results for the jet rise, or so-called 'plume centre-line', defined as the locus of the maximum velocity on each of the planes $x' =$ constant. To a large extent, this variation is attributed to the flow conditions at the jet exit. The jet rise resulting from a hole in a wall shows considerable disagreement with that resulting from a pipe discharge for three essential reasons. First, the momentum distribution (shape factor) of the jet at the time of issuance is different in the two cases. Second, the hole in a wall produces a potential core, adding stiffness and very low turbulence to the initial flow. Third, in the case of a hole in a wall, the vorticity developed in the boundary layer over the wall will roll up in the wake of the jet, in much the same way as in the case of the bound vortex arising from the vorticity rings inside the hole, except that the sign of the rolled-up vorticity will be opposite to that of the bound vortex system. When one faces the cross-stream, downstream of the jet, the left half of the jet ($y' < 0$) will have positive vorticity in the bound vortex, whereas the rolled-up vorticity from the wall boundary layer, spilled around the jet, will be negative, thus making the total circulation less than that of the jet from a simple pipe. Hence the entrainment on the lee side of the jet will be reduced. From a momentum flux argument, reduced entrainment implies a more compliant jet. This explains the difference between the jet rise in the Kamotani & Greber (1972) experiment with a skirted jet and those in the experiments of Hewett *et al.* (1971), Chassaing *et al.* (1974) and the present investigation, performed with a jet from a simple pipe.

From the preceding discussion, one may deduce that the jet's development and asymptotic geometry and state may depend a great deal on the initial flow conditions. Furthermore, since this three-dimensional and strongly vortical flow is as much influenced by the vorticity level as the momentum level, throughout its development, any intrinsic representation of its behaviour must take into

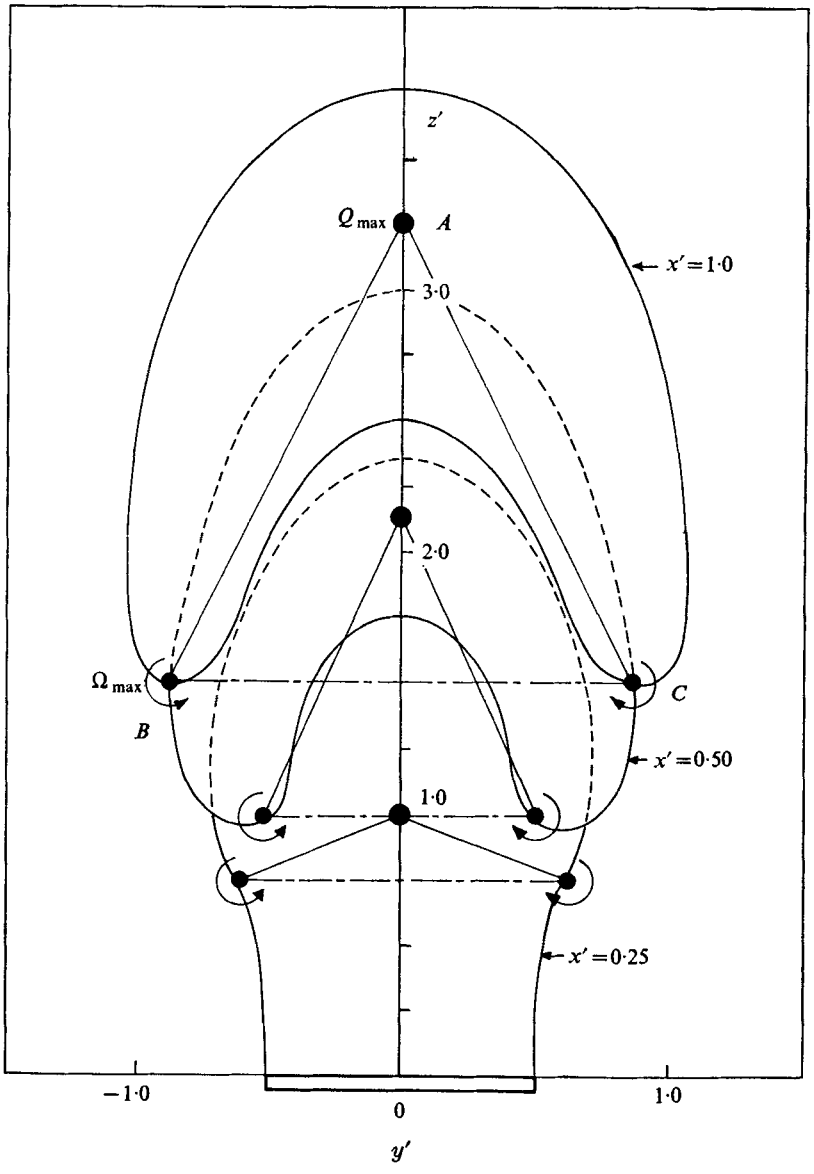

FIGURE 11. Development of jet boundary and locations of Q_{max} and Ω_{max}.

account the vorticity axes as well as the momentum axis. This development is shown in figure 11. Pratte & Baines (1967) were among the first to observe that the vorticity remains strong even at 1000 jet diameters downstream, while the velocity field has nearly decayed at that distance.

Figure 11 shows three successive x' cross-sections of the jet boundaries, as defined by the contour of the ridge of vorticity. The maximum values of the vorticity on that ridge are represented by points B and C. The locus of these points in successive x' planes represents the vorticity axes on both sides of the

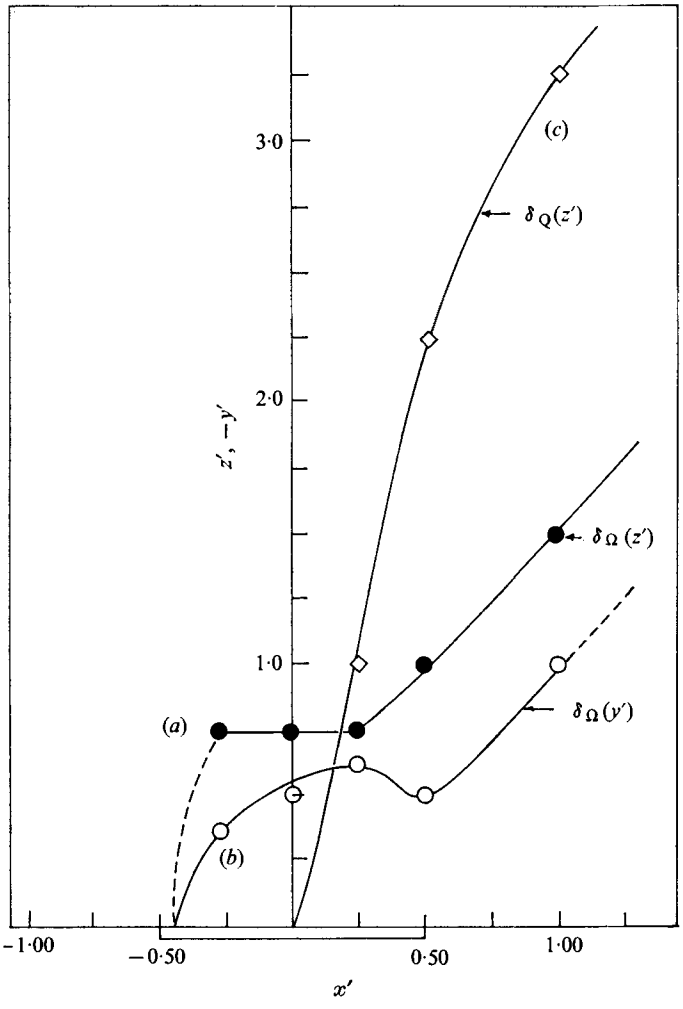

FIGURE 12. Locus of maximum velocity and vorticity centres.

flow. Point A on the figure represents the maximum velocity on each of the planes; and the locus of the points A represents the momentum axis of the jet, or the 'plume centre-line'. We conclude that any intrinsic co-ordinate representation of this flow must include not only the path of the centres A, but also those of B and C. In discussing the development of this flow, it is necessary to discuss the development of the triangle ABC, which represents the intrinsic frame of reference for this flow.

Figure 12 shows the development of these centres in three dimensions. For small U_j/U_∞ and for small distances downstream, since A occurs on the symmetry plane the locus of A, given by δ_Q, is on the x', z' plane and is shown as curve (c) on the figure. The loci of points B and C require a three-dimensional representation. This is why their locations are represented by curve (a), giving $\delta_\Omega(z')$ on the x', z' plane, and by curve (b), giving $\delta_\Omega(y')$ on the x', y' plane.

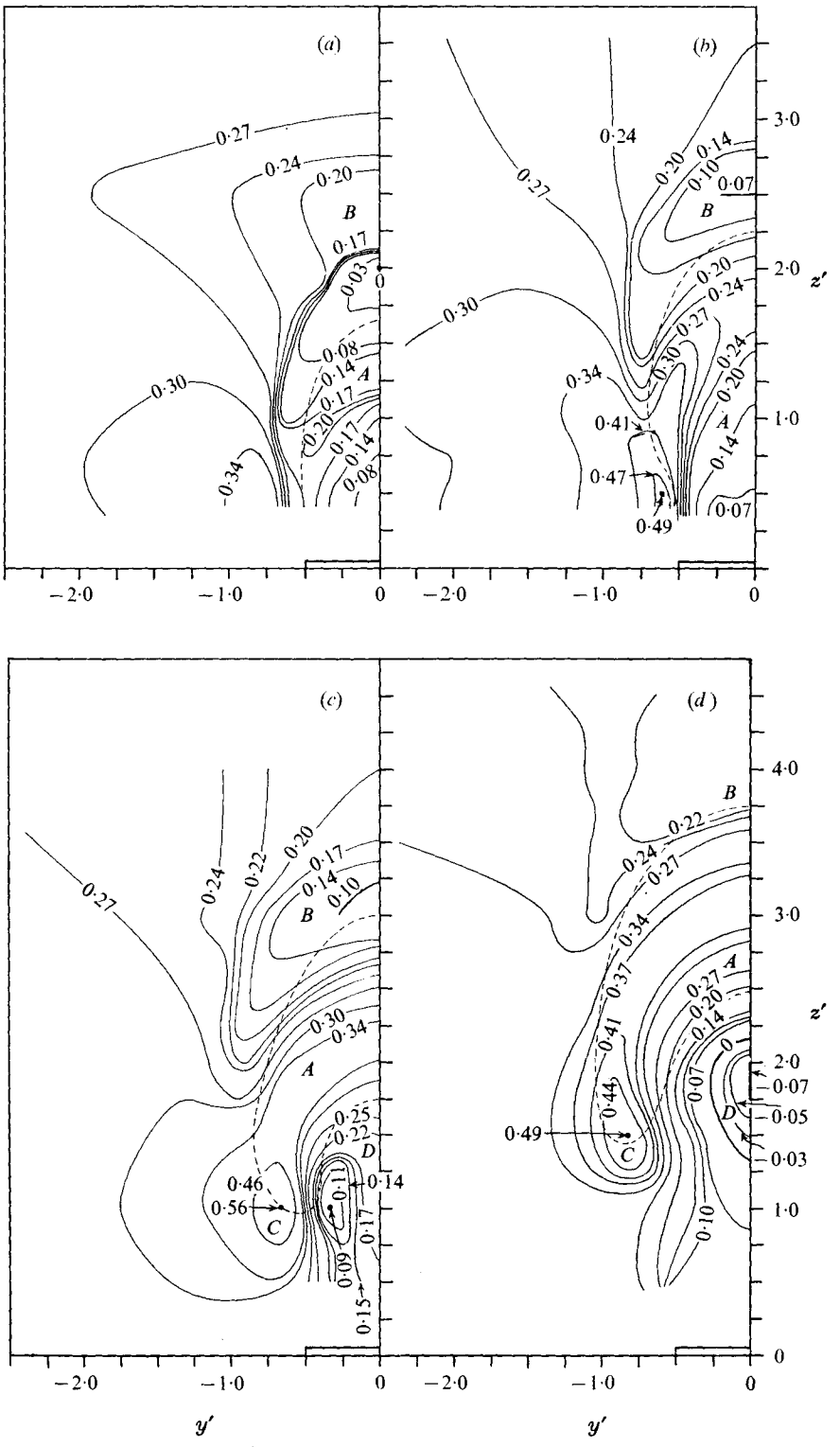

FIGURE 13. Contours of U/U_j. (*a*) $x' = 0$. (*b*) $x' = 0{\cdot}25$. (*c*) $x' = 0{\cdot}50$. (*d*) $x' = 1{\cdot}00$.

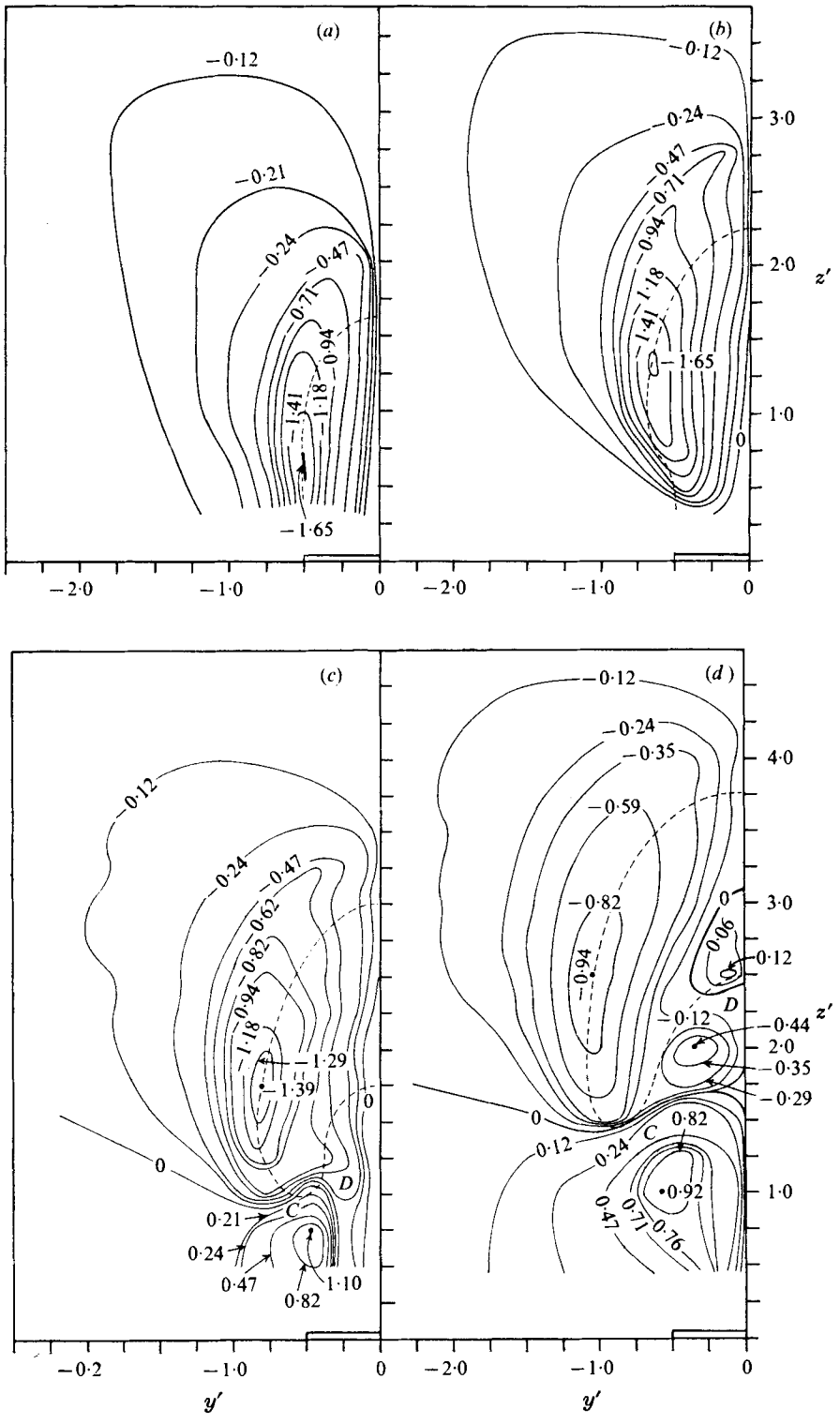

FIGURE 14. Contours of V/U_∞. (*a*) $x' = 0$. (*b*) $x' = 0{\cdot}25$. (*c*) $x' = 0{\cdot}50$. (*d*) $x' = 1{\cdot}00$.

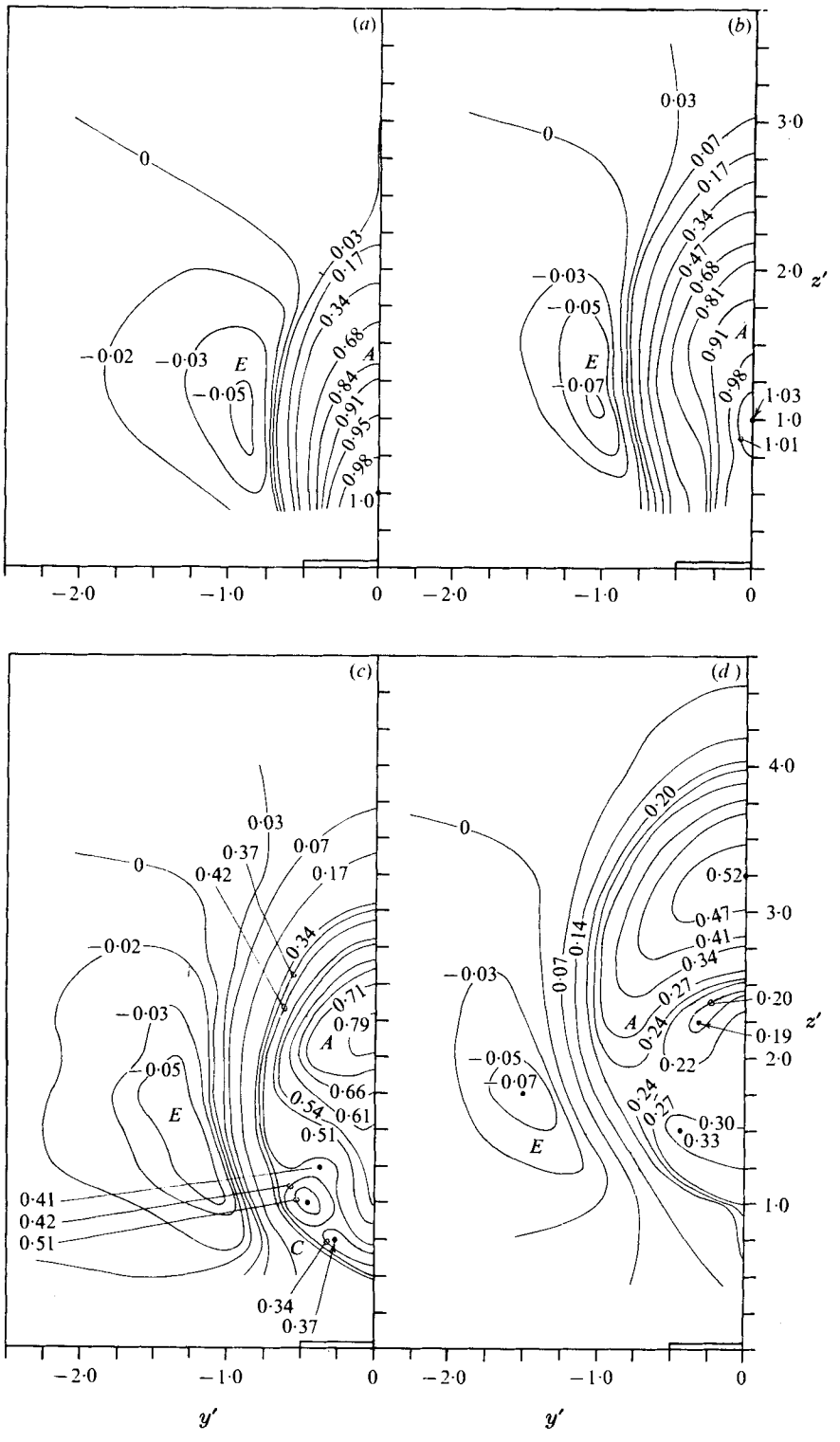

FIGURE 15. Contours of W/U_j. (*a*) $x = 0$. (*b*) $x' = 0{\cdot}25$. (*c*) $x' = 0{\cdot}50$. (*d*) $x' = 1{\cdot}00$.

8. Mean velocity contours

Figures 13, 14 and 15 show contours of U/U_j, V/U_∞ and W/U_j, as well as the jet boundary, for the planes $x' = 0$, 0·25, 0·50 and 1·00. Of the four planes, only the last cuts the jet fully into the wake. It must be recalled that for a three-dimensional flow contours of constant velocity on a given plane are not streamlines. This is one of the fundamental difficulties in the analysis and interpretation of three-dimensional flows.

In these contours one can identify six separate regions of flow. These regions are labelled $A, \ldots, E$ on the figures. In region A one finds the jet flow proper, with high values of W/U_j and low values of U/U_j, particularly in the planes $x' =$ constant closer to the origin. For the planes $x' = 0{\cdot}50$ and 1·00 the jet has already bent sufficiently in the x direction to give rise to larger values of U/U_j, accompanied by smaller values of W/U_j. Region B is that of the cross-stream on the windward side of the jet. This region is characterized by a decrease in U/U_j, as the cross-stream approaches the leading surface of the jet, and is identified by the closed half-contours of U/U_j for larger values of z'. Of the four $x' =$ constant cross-sections shown, the jet is stiffest (largest momenta) at $x' = 0$. On this plane a kind of stagnation point where $U/U_j = 0$ is observed at $z' = 2{\cdot}00$, while $V/U_\infty < 0$ and $W/U_j < 0$, implying that on this stagnation streamline the free stream has decelerated completely in the x direction and its momentum has been converted into momentum in the z direction by the jet. As we look at succeeding planes $x' > 0$, owing to the bending of the jet in the x direction U/U_j is always non-zero in this region (B) and in the plane of symmetry $y' = 0$, and its value increases with increasing x'.

The bound vortex is identified with the region marked C. The contours of U/U_j and V/U_∞ identify this region best. The V/U_∞ contours in figure 14 show flow ($V/U_\infty < 0$) in that region which is inward, i.e. opposite in direction to the remaining (outward) flow. The velocity V has been made dimensionless with U_∞ instead of U_j in order to distinguish the influence of the jet on the free stream. In these contours there appear at $x' = 1{\cdot}00$ other small regions of positive and negative V/U_∞ near $y' = 0$ and $2{\cdot}00 < z' < 3{\cdot}00$. These small regions are attributed to free-stream flow already trapped in the jet through a spiralling motion of the entrainment. Also V/U_∞ changes sign twice and U/U_j becomes negative. The contours of Ω_x in figure 17 (a) show these regions as a reversal of Ω_x. Finally, because of symmetry with respect to the plane $y' = 0$, the non-zero V/U_∞ contours in figure 14 do not cross the ordinate. The image contours with opposite sign should be present on the $y' > 0$ side of the flow.

As the free stream moves around the surface of the jet, increasing its velocity, it is also deflected in the z' direction. This region (E) is distinguishable in figure 15 and in the vorticity contours in figure 17 (a). The $-z'$ motion is the induced effect of the bound vortex, which generates a counter-rotating motion in the free stream.

9. Mean vorticity contours

The mean vorticity components were calculated from the velocity field by evaluating the circulation per unit area on planes normal to the co-ordinate system in the fine grid array of figure 5. The mean vorticity vector's magnitude $|\boldsymbol{\Omega}|$ and components Ω_x, Ω_y and Ω_z divided by the mean vorticity at the pipe exit, $\Omega_j = 2570\,\mathrm{s}^{-1}$, are plotted in figures 16–19. Figures 16 and 17(*d*) were used as a basis for defining the characteristic boundary of the jet. Since the last plane investigated was $x' = 1{\cdot}00$, Ω_x was the only component that could be calculated on that plane. The vorticity ridge on each of the x' planes was taken as the characteristic boundary of the jet. This is felt to be a more defensible definition than a boundary defined through the mean velocity contours as suggested, for instance, by Keffer & Baines (1973), Jordinson (1956) and Slawson & Csanady (1967). Moussa (1976) has shown through a sequence of figures similar to figure 10 that the boundary based on the vorticity ridge correlates well with the turbulence intensity ridge. As in the case of the velocity contours, a vorticity contour is not necessarily a vortex line. However, the points of maximum vorticity at every x' do seem to represent the same vortex line, as evidenced by three-dimensional vector plots.

At the pipe exit and on the plane $x' = 0$, the lines of constant vorticity $|\boldsymbol{\Omega}|/\Omega_j$ are parallel to the pipe walls. If it were not for the bending and diffusion of the jet, these lines would remain parallel. In figure 16(*a*), at $x' = z' = 0$, these lines start parallel to the pipe wall. Because of the stretching and tilting due to diffusion and the action of the cross-stream, the upper ends of the contour lines at $x' = 0$ begin to close. In subsequent planes, $x' = 0{\cdot}25$ and $0{\cdot}50$, these contours begin to close at the lower end in an anticlockwise direction, forming the bound vortex on the $y' < 0$ side of the flow. In figure 16(*c*) the point M is the point of maximum vorticity, located at the trailing edge of the lobe of the jet boundary. Around M, the closed contours of vorticity, of the order of the jet-exit mean vorticity, identify the location of the bound vortex. The trend of this formation can be noticed even earlier at $x' = 0{\cdot}25$, when the flow is presumably strongly dependent on the pipe exit conditions. In the near-field planes, the largest share of the mean vorticity is in the z direction because of the severity of the tilting of the vortex lines. This is evident on comparing the values in figures 16 and 19. In figure 16, the vorticity contours of the external flow, to the left of the jet boundary, diverge on the windward side of the jet surface and converge rapidly on the lee side of this surface. The divergence is due to the deceleration of the cross-stream, followed by compression of the vortex lines, whereas the convergence is due to the acceleration of the cross-stream on the lee side of the jet boundary, which is accompanied by a stretching of the vortex lines.

Other important behaviour may be seen in figure 17. Because the Ω_x emanating from the pipe is opposite in sign in the two halves of the pipe, Ω_x/Ω_j distributions will not cross the plane of symmetry. If it were not for the bending of the jet, on figure 17(*a*), at $x' = 0$ the values of Ω_x/Ω_j would constitute the values of the total vorticity. As the boundary layer in the pipe has positive vorticity in the half-space $y' < 0$, so do the values of Ω_x/Ω_j and Ω_z/Ω_j in the jet.

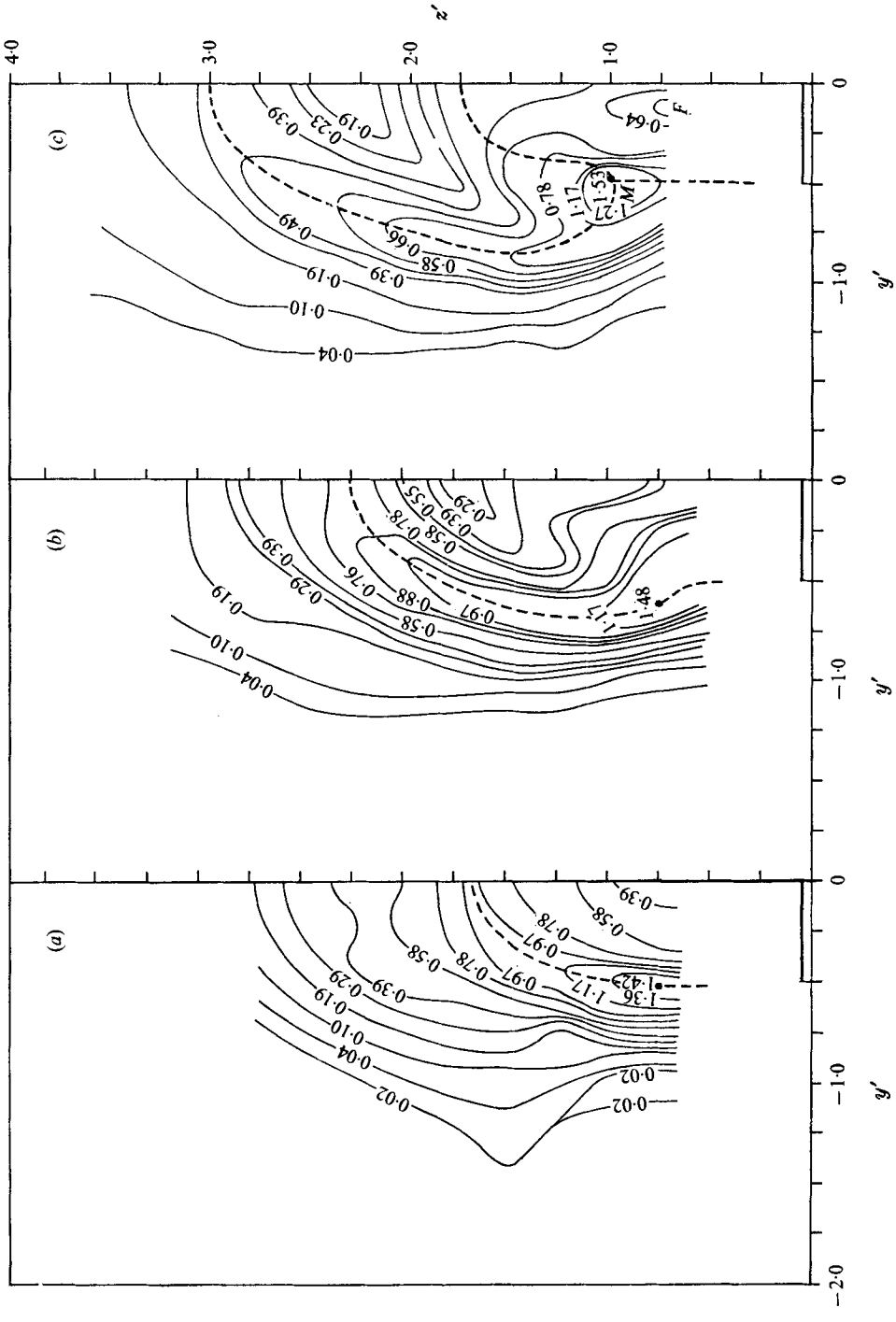

FIGURE 16. Contours of $|\Omega|/\Omega_j$. (*a*) $x' = 0$. (*b*) $x' = 0{\cdot}25$. (*c*) $x' = 0{\cdot}50$.

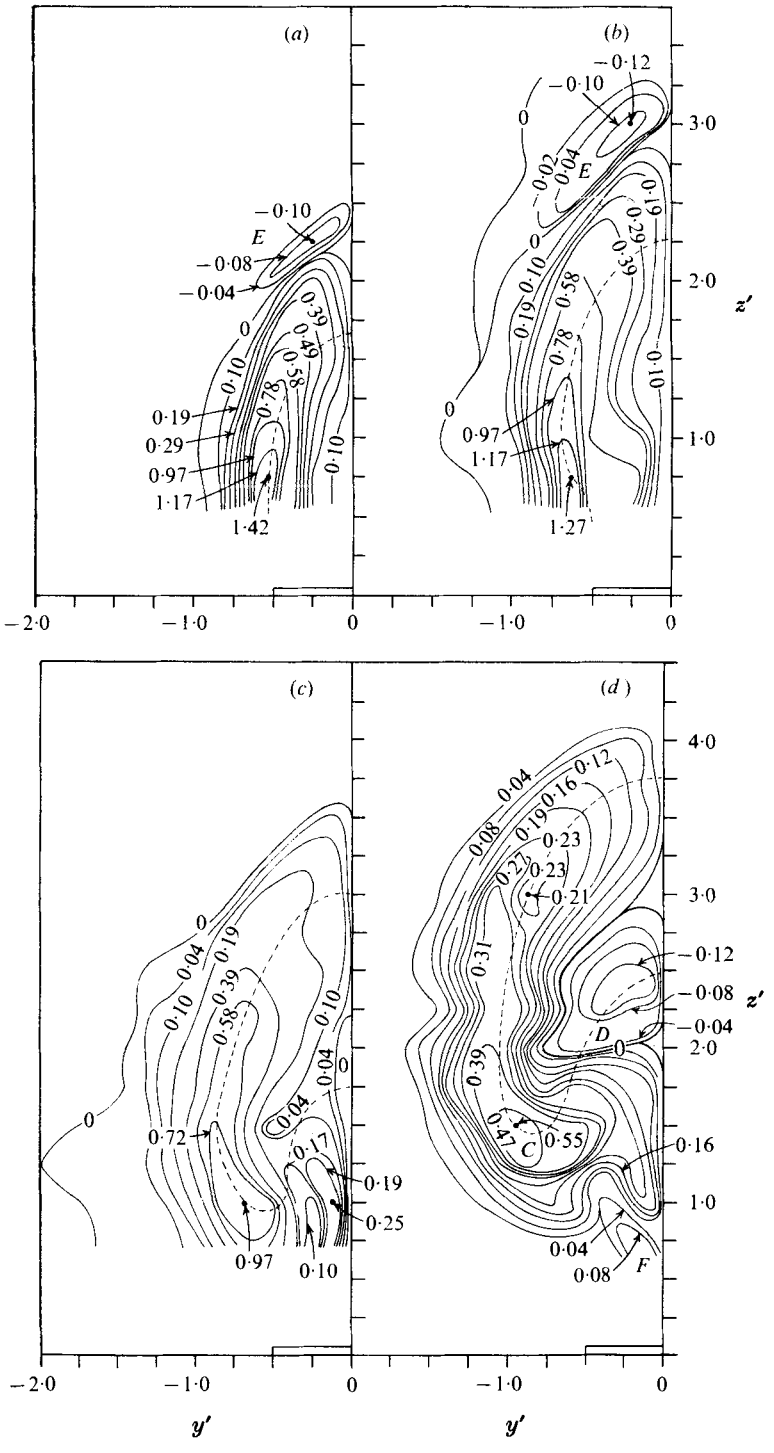

FIGURE 17. Contours of Ω_x/Ω_j. (*a*) $x' = 0$. (*b*) $x' = 0{\cdot}25$. (*c*) $x' = 0{\cdot}50$. (*d*) $x' = 1{\cdot}00$.

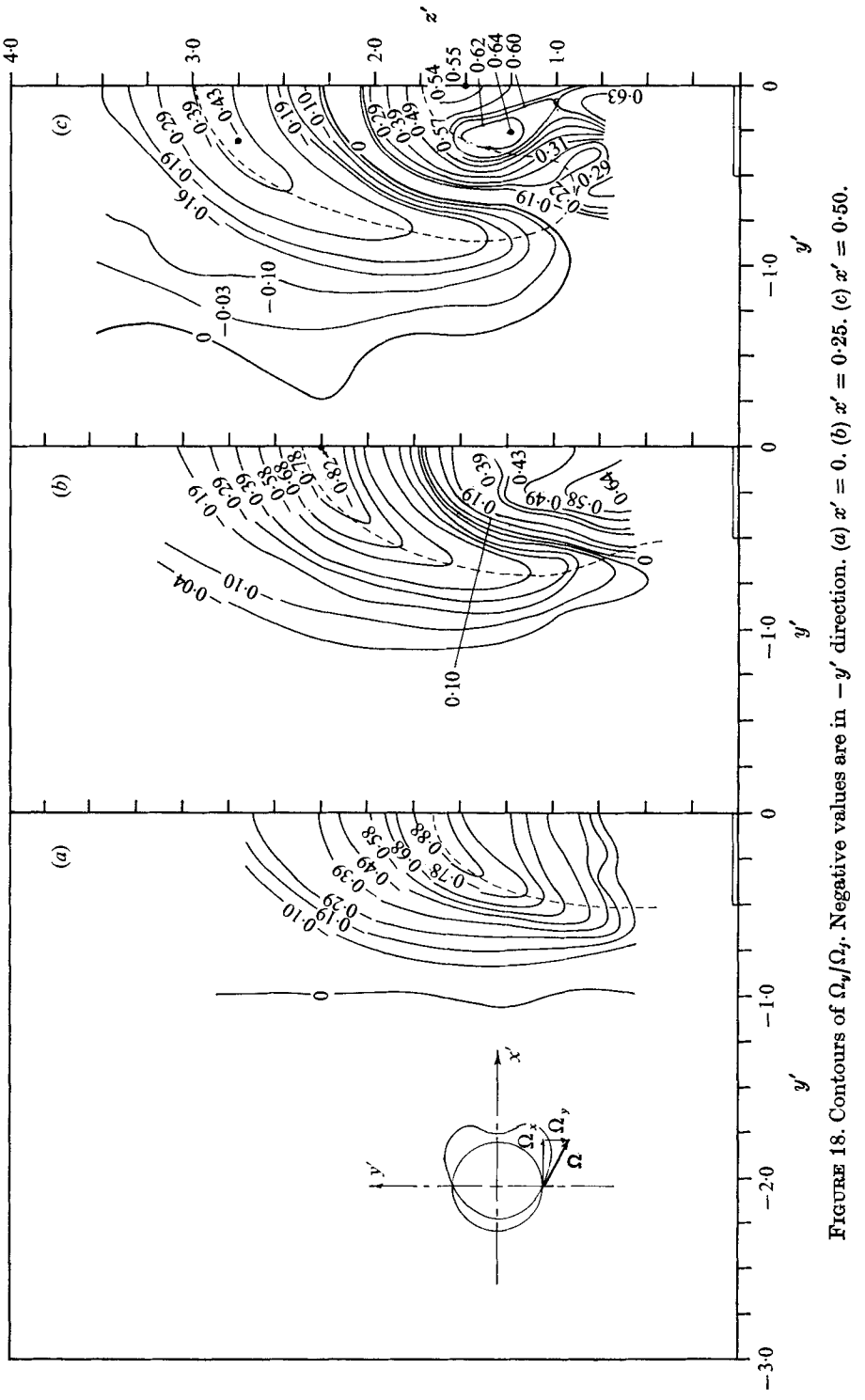

FIGURE 18. Contours of Ω_y/Ω_j. Negative values are in $-y'$ direction. (*a*) $x' = 0$. (*b*) $x' = 0{\cdot}25$. (*c*) $x' = 0{\cdot}50$.

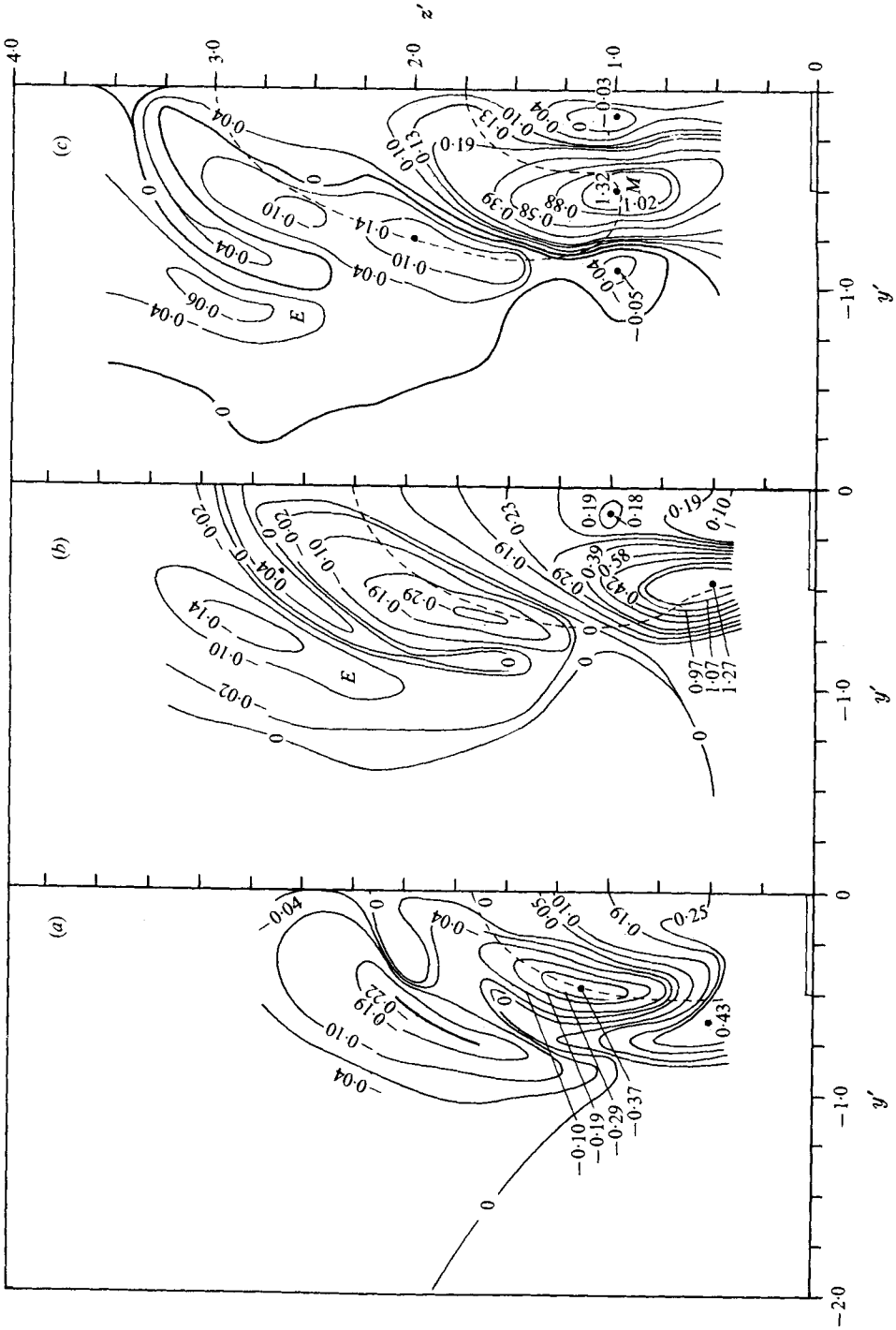

FIGURE 19. Contours of Ω_z/Ω_j. (*a*) $x' = 0$. (*b*) $x' = 0{\cdot}25$. (*c*) $x' = 0{\cdot}50$.

It was mentioned in the previous section that the cross-stream develops an induced negative vorticity in all three directions as it spills over the jet boundaries. When one takes a very large contour around the entire flow such that the legs of the contour are in irrotational flow, we can deduce that each bound vortex must generate in the cross-stream an equal and opposite rotation with equal circulation. The presence of this induced flow with negative Ω_x/Ω_j and Ω_z/Ω_j around the leading surface of the jet boundary can be seen in figures 17(*a*) and 19. Figure 17(*d*), for the plane $x' = 1{\cdot}00$, is the only distribution that gives the full cross-section of the jet and its wake. On that figure we can see the bound vortex, marked *C*, the location of the entrained fluid, marked *D*, and the location of the wake proper, marked *F*.

In figure 18, at $x' = 0$, if the jet had not bent, Ω_y would have been zero everywhere, because the total vorticity vector would have been in the x direction. The fact that $\Omega_y < 0$ for most of the flow can be explained with the help of the sketch of a typical vortex-tube cross-section drawn on this figure. The bending in the x direction, the faster transverse growth in the y direction and the resulting loss of axial symmetry explain why $\Omega_y \neq 0$ at $x' = 0$. On figures 18(*b*) and (*c*), two distinct regions begin to appear, depending on the sign of Ω_y. The regions with positive values are those of wake entrainment and the wake proper. The region of negative values represents the rest of the flow.

The original flows inside the pipe and upstream cross-stream are completely devoid of z vorticity. The appearance of mean z vorticity as seen in figure 19 can only be explained by tilting and stretching of the vorticity in the other two directions and by the action of the Reynolds stresses. For reasons already discussed, the cross-stream, as it deflects around the leading jet surface, acquires negative Ω_z. In figure 19 the bundling process that forms the bound vortex is seen clearly, and the values of Ω_z in that tube is positive. By the time the flow reaches the plane $x' = 0{\cdot}50$, the maximum value of Ω_z/Ω_j is nearly that of the maximum total vorticity in figure 16. On dividing these two maximum values of Ω_z and $|\boldsymbol{\Omega}|$, the angle in the x, z plane between the maximum vorticity vector, at $x' = 0{\cdot}50$, and the x axis is found to be nearly 60°, which is in close agreement with the 50° shown in figure 12. In fact, this correspondence of the direction of the vorticity vector and the orientation of the locus of the maximum vorticity at successive planes $x' =$ constant is fair in the confines of the near field, and supports the concept that the bound vortex is an extension of the vorticity rings emanating from the pipe.

10. The mean vorticity flux

The mean vorticity equation in three dimensions can be written in an integral form more convenient for the calculation of the net flux of mean vorticity:

$$\boldsymbol{\phi}_\Omega = \oint_S \boldsymbol{\Omega}(\mathbf{Q}\,.\,d\mathbf{S}) = \oint_S \mathbf{Q}(\boldsymbol{\Omega}\,.\,d\mathbf{S}) - \int_V \overline{(\mathbf{q}\,.\,\nabla)\boldsymbol{\omega}}\,dV + \int_V \overline{(\boldsymbol{\omega}\,.\,\nabla)\,\mathbf{q}}\,dV + \nu \oint_S \nabla\boldsymbol{\Omega}\,.\,d\mathbf{S}, \tag{7}$$

where $\mathbf{Q}$, $\boldsymbol{\Omega}$ and $\mathbf{q}$, $\boldsymbol{\omega}$ are the time-mean and time-dependent (fluctuating) values of the velocity and vorticity vectors respectively. In essence (7) is a Reynolds-type

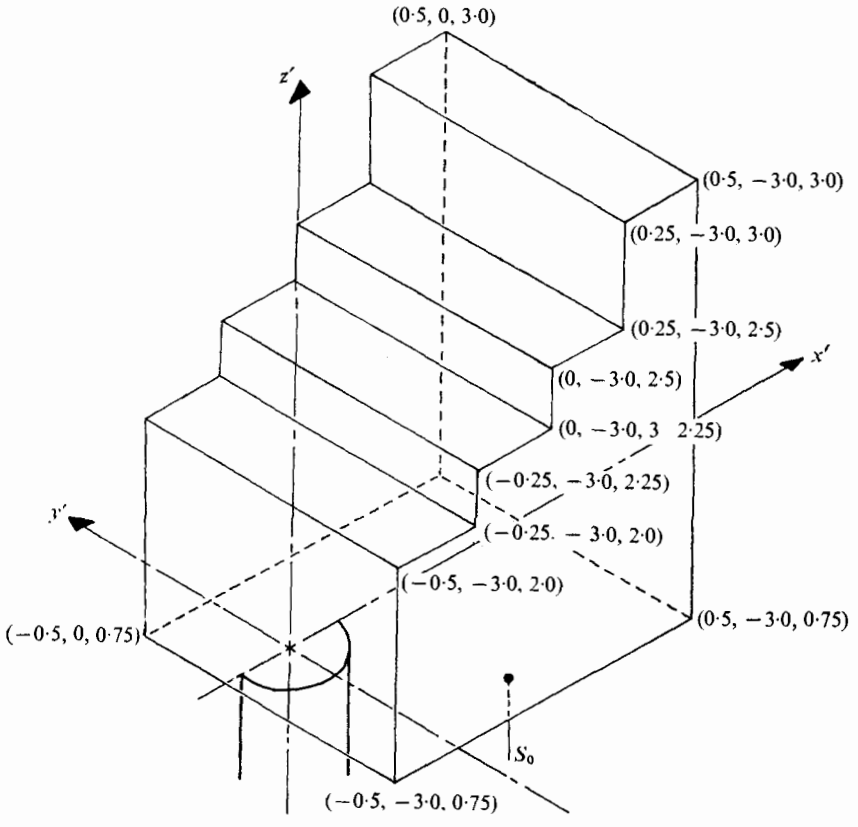

FIGURE 20. Control surfaces for calculation of flux.

vorticity flux equation integrated over a finite control volume V with bounding surface S, shown in figure 20. The integral on the left side of this equation is the net flux of mean vorticity across the closed surface. The first term on the right is the change in vorticity flux caused by the stretching and tilting of the mean vorticity. The second and third terms are Reynolds-type terms, which in this strong turbulent field contribute significantly to the transport, stretching and tilting of the turbulent vorticity produced by the Reynolds stresses. The last term, the molecular diffusion of the mean vorticity flux, is negligible compared with the other terms.

The vorticity flux in this flow is compared with the mean vorticity flux emanating from the pipe in the form of vortex rings distributed across the pipe cross-section. This is because they are part of the same system. At the pipe exit the vorticity is everywhere in the x, y plane; hence, because of symmetry the resultant vector vorticity flux through the exit cross-section is zero. Consequently, the flux that has been chosen for comparison purposes is of absolute magnitude $|\boldsymbol{\Omega}| = dW/dr$. Then

$$2\phi_{\Omega j} = \pi \int_0^{\frac{1}{2}D} r d(W^2) \tag{8}$$

$\int\Omega_x(\mathbf{Q}.d\mathbf{S})$	$\int\Omega_y(\mathbf{Q}.d\mathbf{S})$	$\int\Omega_z(\mathbf{Q}.d\mathbf{S})$	$\int U(\boldsymbol{\Omega}.d\mathbf{S})$	$\int V(\boldsymbol{\Omega}.d\mathbf{S})$	$\int W(\boldsymbol{\Omega}.d\mathbf{S})$	
$\phi_{\Omega j}$	$\phi_{\Omega j}$	$\phi_{\Omega j}$	$\phi_{\Omega j}$	$\phi_{\Omega j}$	$\phi_{\Omega j}$	
—	—	—	—	0·289	—	In } Closed
0·284	0·169	0·080	0·527	—	0·410	Out } surface
0·422	—	0·238	0·136	—	0·238	In } Surface
—	0·044	—	—	0·070	—	Out } S_0

$|\oint\boldsymbol{\Omega}(\mathbf{Q}.d\mathbf{S})| = 0{\cdot}34\phi_{\Omega j}$, $|\oint\mathbf{Q}(\boldsymbol{\Omega}.d\mathbf{S})| = 0{\cdot}73\phi_{\Omega j}$, $|\oint\boldsymbol{\Omega}(\mathbf{Q}.d\mathbf{S}) - \oint\mathbf{Q}(\boldsymbol{\Omega}.d\mathbf{S})| = 0{\cdot}61\phi_{\Omega j}$

TABLE 2. Mean vorticity flux across the control surfaces of the half-flow. Components of terms in (7). All values divided by $\phi_{\Omega j} = 16{\cdot}6\ \mathrm{m^3/s^2}$.

defines $\phi_{\Omega j}$. From the measured values of W at the pipe exit, this flux is calculated to be $33{\cdot}2\ \mathrm{m^3/s^2}$ for the whole jet. The mean vorticity flux in half of the flow, $16{\cdot}6\ \mathrm{m^3/s^2}$, given in table 1, is the value used in table 2, which shows the balance (7). From this value divided by U_j and the area of the pipe, we obtained a value of the spatial mean vorticity at the pipe exit, $\Omega_j = 2570\,\mathrm{s^{-1}}$, which has been used to make the vorticity values in this paper dimensionless. The vector sum of the vorticity fluxes in *half of the pipe* differs from $\phi_{\Omega j}$ by a factor of $\frac{1}{2}\pi$ and is found to be $10{\cdot}6\ \mathrm{m^3/s^2}$; see table 1.

Besides showing the balance (7), table 2 shows the contribution to the flux integrals made by the plane $z' = 0{\cdot}50$ through the surface S_0, providing additional evidence of the very rapid development of Ω_z shown by the fact that the vortex advection and stretching and tilting, given in the third and sixth columns of table 2, are comparable in magnitude to the contribution from Ω_x advection, given in the first column.

The tilting and stretching term $\oint\mathbf{Q}(\boldsymbol{\Omega}.d\mathbf{S})$ was initially zero everywhere at the pipe exit, whereas by the time the flow reached the plane $x' = 1{\cdot}00$ it had a value 73 % of that of the total mean vorticity flux in the pipe. This shows again the importance of the deformation of the vortex rings emanating from the pipe. The balance (7) indicates that 61 % of the mean vorticity originally in the pipe is converted into turbulent vorticity up to $x' = 1{\cdot}00$, which means that the flux of turbulent vorticity is of the same order as that of the mean vorticity.

An alternative approach to this conclusion comes from an independent estimate of the ratio of the flux per unit area of turbulent vorticity to the flux per unit area of mean vorticity distributed in a typical region of this flow field. These distributions are shown in figure 21 along the symmetry line $y' = 0$ at $x' = 0{\cdot}50$. Distributions (*a*) and (*b*) are those of the turbulent vorticity $\langle q\rangle/\lambda\Omega_j$ and the mean vorticity $|\boldsymbol{\Omega}|/\Omega_j$, where λ is the microscale in the mean direction of the flow, while $\langle q\rangle/\lambda$ is a measure of the root mean square of the turbulent vorticity. Thus we conclude that in this region chosen for comparison the turbulent vorticity is approximately three times the magnitude of the mean vorticity. Now the flux per unit area of turbulent vorticity will be $\overline{q^2}/\lambda\Omega_j$ at every z'. The comparable flux per unit area of the mean vorticity will be $Q|\boldsymbol{\Omega}|/\Omega_j$. Before comparing these two distributions of flux per unit area we divide both expressions by Q, so that we can compare $\overline{q^2}/\lambda Q\Omega_j$ and $|\boldsymbol{\Omega}|/\Omega_j$ instead. Thus

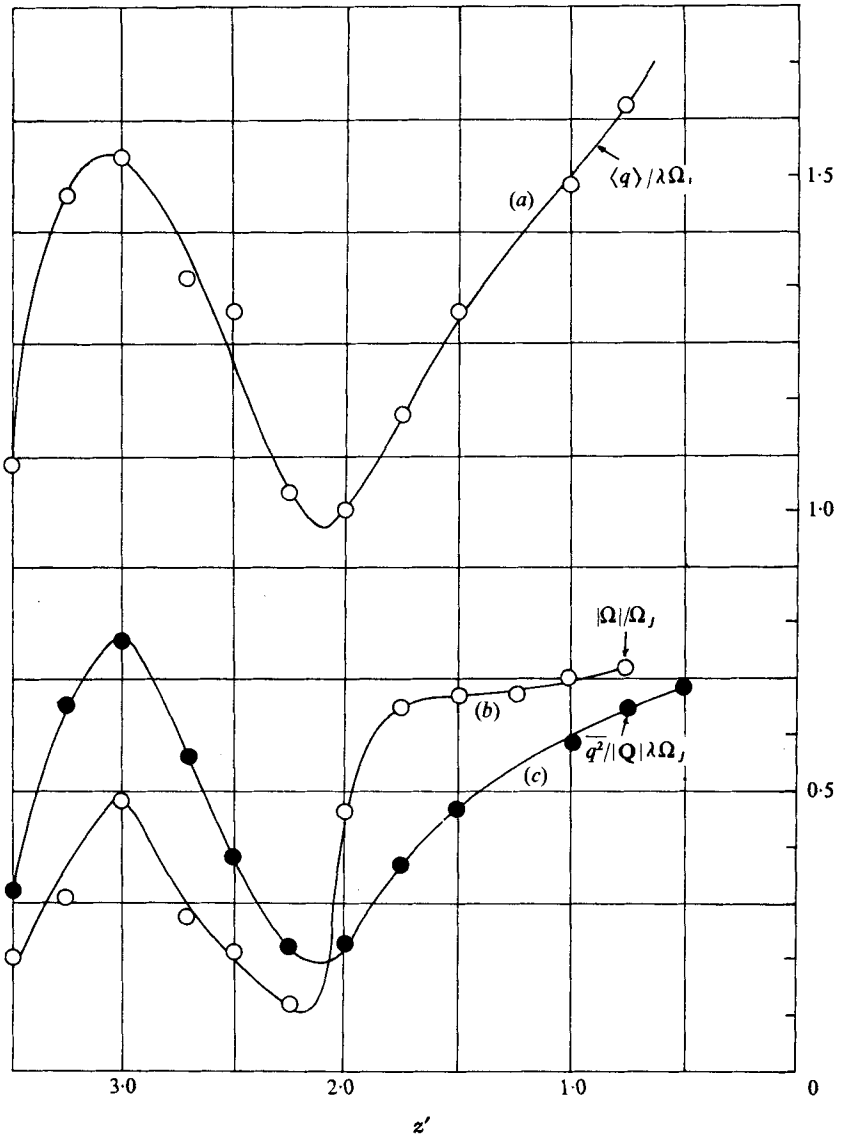

FIGURE 21. Comparison of vorticity and vorticity flux along $y' = 0$ at $x' = 0{\cdot}50$.

comparison of curves (b) and (c) is equivalent to comparison of the fluxes per unit area of turbulent and mean vorticity. This comparison shows, first, that the two are of the same order as predicted by the previous argument concerning the total fluxes, and second, that at the jet boundary ($z' \simeq 2{\cdot}25$) the ratio of the turbulent vorticity flux to the mean vorticity flux changes from a value less than unity in the wake to a value larger than unity in the jet proper.

11. Conservation laws: mass, momentum and circulation

From the digitized data on velocity and vorticity for the array of measured points in the control volume in figure 20, the mass flux and circulation were calculated for this isochoric flow, in order to have a precise global estimate of the accuracy of the measurements as well as of the numerical method. The mass flux across all the surfaces of the control volume balanced to within 2 %, and the circulation balanced to within 2·4 %. This we believe to be excellent considering the level of turbulence in many parts of the flow.

The momentum fluxes across the same surfaces were also calculated. An average radial pressure gradient $\Delta P/\Delta\kappa$ and the radius of curvature of the jet within the near field investigated were calculated to be 460 N/m^3 and 2 m respectively.

12. Conclusions

The leading surface of the jet, acting as a barrier to the cross-flow, is quantitatively very close to that of a rigid cylinder. For a jet issuing from an unskirted cylindrical pipe, the shed vortices are continuous with those in the pipe, and are characteristic of the pipe.

It is proposed that, in addition to the jet's maximum-velocity centre-line, the axes of maximum vorticity joining the centres of the bound vortices be considered equally in the development of the flow. A new, more physical definition of the jet boundary is proposed.

The major part of the change from complex lamellar flow in the pipe to a Beltrami flow in the jet takes place in the near field, within a few pipe diameters from the pipe exit. It is proposed that the bound vortices are extensions of the vorticity rings emanating from the pipe.

The analysis of the vorticity flux shows that the turbulent vorticity is of the same order of magnitude as the mean vorticity, and that the mean tilting and stretching vorticity flux at one diameter downstream is about 75 % of the total mean vorticity flux at the pipe exit.

REFERENCES

BOSANQUET, C. & PEARSON, J. L. 1936 The spread of smoke and gases from chimneys. *Trans. Faraday Soc.* **32**, 1249.

CHASSAING, P., GEORGE, J., CLARIA, A. & SANANES, F. 1974 Physical characteristics of subsonic jets in a cross-stream. *J. Fluid Mech.* **62**, 41.

CHOPRA, K. P. & HUBERT, L. F. 1964 Kármán vortex streets in earth's atmosphere. *Nature*, **203**, 1341.

ESKINAZI, S. 1975 *Fluid Mechanics and Thermodynamics of our Environment*, p. 316. Academic.

FANKHAUSER, J. C. 1971 Thunderstorm–environment interactions determined from aircraft and radar observations. *Mon. Weather Rev.* **99**, 171.

FAY, J. A. 1973 Buoyant plumes and wakes. *Ann. Rev. Fluid Mech.* **5**, 151.

FUJITA, T. & GRANDOSO, H. 1968 Split of a thunderstorm into anticyclonic and cyclonic storms and their motion as determined from numerical model experiments. *J. Atmos. Sci.* **25**, 416.

HEWETT, T. A., FAY, J. A. & HOULT, D. P. 1971 Laboratory experiments of smoke stack plumes in a stable atmosphere. *Atmos. Environ.* **5**, 767.

HOLLAND, J. Z. 1953 A meteorological survey of the Oak Ridge area. *Oak Ridge Nat. Lab., Tennessee, Rep.* USAEC ORO-99.

JORDINSON, R. 1956 Flow in a jet directed normal to the wind. *Aero. Res. Counc. R. & M.* no. 3074.

KAMOTANI, Y. & GREBER, I. 1972 Experiments on a turbulent jet in a cross flow. *A.I.A.A. J.* **10**, 1425,

KEFFER, J. F. & BAINES, W. D. 1973 The round turbulent jet in a cross-wind. *J. Fluid Mech.* **15**, 481.

LAIKHTMAN, D. L. 1961 Physics of the boundary layer of the atmosphere. *GIMIZ Gidrometeorol. Izdatel'stvo, Leningrad*, p. 189.

LUCAS, D. H. 1958 The atmospheric pollution of cities. *Int. J. Air Pollution*, **1**, 71.

MCALLISTER, J. D. 1968 A momentum theory for the effects of cross flow on incompressible turbulent jets. Ph.D. dissertation, University of Tennessee.

MCMAHON, H. M., HESTER, D. D. & PALFREY, J. G. 1971 Vortex shedding from a turbulent jet in a cross-wind. *J. Fluid Mech.* **48**, 73.

MORTON, B. R., TAYLOR, G. I. & TURNER, J. S. 1956 *Proc. Roy. Soc.* A **234**, 1–23.

MOUSSA, Z. 1976 The near field flow of an axisymmetric jet in a cross-stream. Ph.D. dissertation, Syracuse University.

PRATTE, B. D. & BAINES, W. D. 1967 Profiles of the round turbulent jet in a cross flow. *J. Hydraul. Div. A.S.C.E.* HY6, 53.

PRIESTLEY, C. H. B. 1956 A working theory of the bent-over plume of hot gas. *Quart. J. Met. Soc.* **82**, 165.

SLAWSON, P. R. & CSANADY, G. T. 1967 On the mean path of buoyant, bent-over chimney plumes. *J. Fluid Mech.* **28**, 311.

SUTTON, O. G. 1932 *Proc. Roy. Soc.* A **135**, 143.

THORARINSSON, S. & VONNEGUT, B. 1964 Whirlwinds produced by the eruption of Surtsey Volcano. *Bull. Am. Met. Soc.* **45**, 440.

TURNER, J. S. 1969 Buoyant plumes and thermals. *Ann. Rev. Fluid Mech.* **1**, 29.

WHITTINGHAM, H. E. 1959 Fire whirlwinds at Imbil. *Austr. Met. Mag.* **25**, 59.

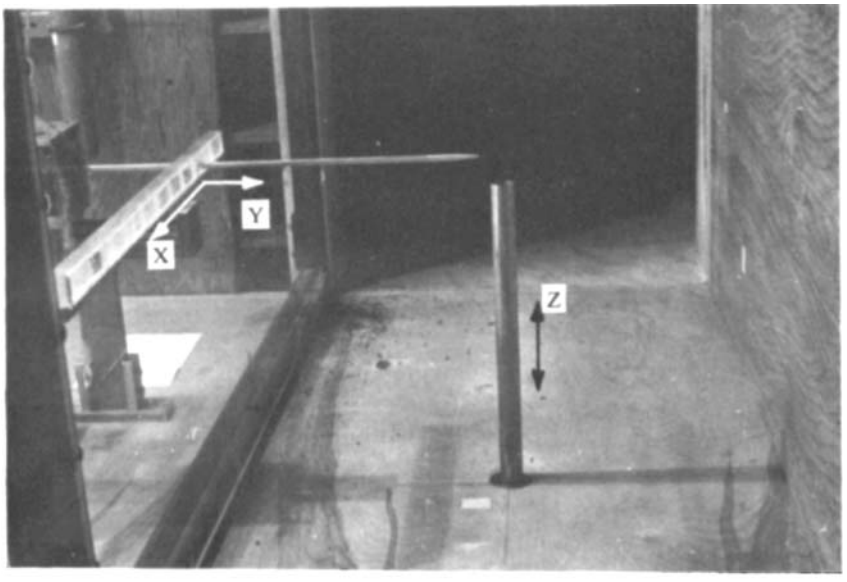

(*a*)

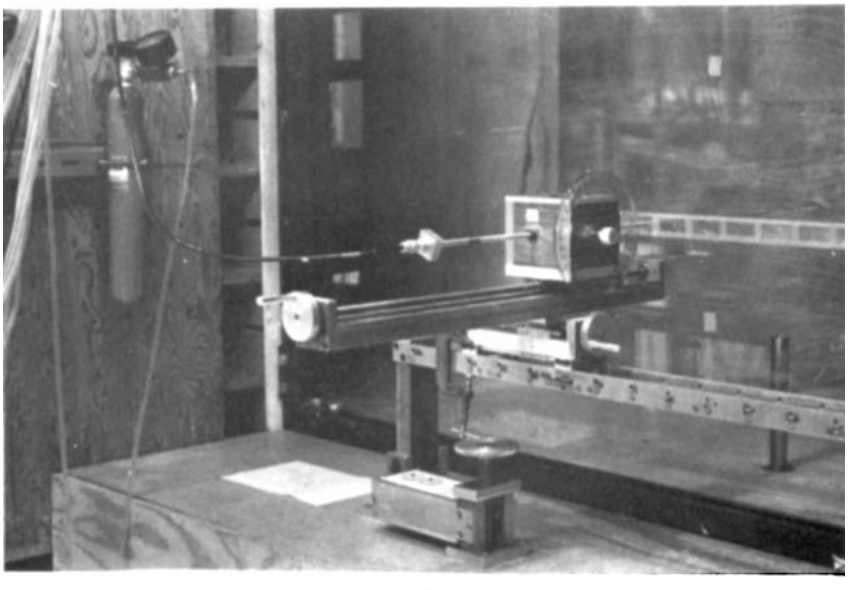

(*b*)

FIGURE 4. (*a*) The jet in the cross-stream and (*b*) the traversing system.